American Mineralogist, Volume 110, pages 791–807, 2025

Heterogeneous distribution of Al-hematite regulated by hydrologic regime in a basaltic laterite of Hainan Island, South China: Implications for the aqueous history of Mars

XIAORONG QIN[1,2,3], WEI TAN[1,2,*], HONGPING HE[1,2,3], JIACHENG LIU[4,5], QI TAO[1,2,†], JIANXI ZHU[1,2,‡],
HONGYAN WEI[1,2,3], LIANYING LUO[1,2,3], KEYAN CHEN[1,2,3], TIANQI ZHANG[1,2,3], AND SHICHAO JI[1,2,§]

[1]State Key Laboratory of Deep Earth Processes and Resources, Guangzhou Institute of Geochemistry/ Guangdong Provincial Key Laboratory of Mineral Physics and Materials, Guangzhou Institute of Geochemistry, Chinese Academy of Sciences, Guangzhou 510640, China
[2]CAS Center for Excellence in Deep Earth Science, Guangzhou 510640, China
[3]University of Chinese Academy of Sciences, Beijing 100049, China
[4]Department of Earth Sciences and Laboratory for Space Research, the University of Hong Kong, Hong Kong, China
[5]NWU-HKU Joint Center of Earth and Planetary Sciences, Department of Earth Sciences, the University of Hong Kong, Pokfulam Road, Hong Kong, China

ABSTRACT

Al-hematite occurs in a wide range of terrestrial soils, but the impact of hydrologic factors on the formation and preservation of Al-hematite remains uncertain. Experimental studies indicate that the ratio of the intensity (I) of the (110) reflection to the intensity of the (104) reflection [(I(110)/I(104)] increases with increasing Al content in a series of synthetic Al-hematite analyzed by X-ray diffraction (XRD), whereas the ratio of the full-width at half maximum (W) of the (110) reflection to the full-width at half maximum of the (104) reflection [W(110)/W(104)] decreases. Quantitative constraints were applied to determine the various levels of Al-substituted hematite in a basaltic laterite (a 48-m-long drill hole) from Hainan Island in South China. The spatial correlation between the distribution of hematite with varying Al content and the location of the groundwater table in the basaltic laterite indicates that hydrologic conditions play a crucial role in regulating the formation and preservation of Al-hematite. The weathering of basalt in a stable water-saturated environment with a relatively slower flow rate promotes the formation of Al-poor hematite. Conversely, the formation of Al-rich hematite was favored by a relatively high flow rate and alternating wet and dry conditions above the groundwater table. Additionally, capillary water in the surficial soil facilitates the expulsion of Al during the recrystallization of Al-rich hematite, resulting in the formation of Al-poor hematite in the surficial soil. Observations from landed instruments and ground-based telescopes have led to the longstanding suspicion that Al-hematite exists on the surface of Mars. The potential presence of Al-hematite in certain martian outcrops may suggest the existence of transient liquid water with slightly higher flow rates, such as episodic floods, emphasizing the dynamic hydrologic conditions on Mars. Moreover, this study suggests that visible and near-infrared (VNIR) spectroscopy can be employed to identify and characterize Al-rich hematite. This approach could be employed to assess the potential presence of Al-rich hematite on Mars, aiding in the study of the planet's hydrologic environment.

Keywords: Al-hematite, basaltic laterite, hydrologic environments, visible and near-infrared spectroscopy, Mars

INTRODUCTION

Hematite (α-$Fe_2^{3+}O_3$) is one of the most ubiquitous iron oxides on the surface of both Earth and Mars (Torrent et al. 1982; Schwertmann et al. 2000b; Cornell and Schwertmann 2003; Fraeman et al. 2013; Hu et al. 2016; Rampe et al. 2020; Jiang et al. 2022). Hematite has the same crystal structure as corundum (α-Al_2O_3) (Jiang et al. 2022). It is well established that certain cations, including Al^{3+}, Cr^{3+}, and Ti^{4+}, can be incorporated into the hematite structure by replacing Fe^{3+} (Schwertmann et al. 1979; Wells et al. 1999). Among these cations, Al^{3+} substitution is the most prevalent, with the capability to substitute for up to 18 mol% of Fe^{3+} in hematite (Schwertmann and Murad 1988; Li et al. 2016). Notably, Al substitution in hematite can have significant effects on its mineralogical characteristics, including color, magnetic properties, crystallinity, and crystal morphology (Barron et al. 1984; Cornell and Schwertmann 2003; Hu et al. 2016; Li et al. 2016; Jiang et al. 2022).

Al-hematite is found in various terrestrial soils (Singh and Gilkes 1992; Jiang et al. 2022), particularly those developed from mafic materials, such as the lateritic soils of southwestern Australia (Singh and Gilkes 1992). Hematite exhibiting unique mineralogical characteristics has also been discovered on the surface of Mars, e.g., nanophase, red crystalline, and gray crystalline hematite (Morris et al. 1989; Bell et al. 1993; Christensen et al. 2001; Catling and Moore 2003; Barron et al. 2006; Fraeman et al. 2013; Rampe et al. 2020). Although definitive proof of Al-rich hematite on Mars is yet to be established, Al substitution remains a

---

* Corresponding author E-mail: tanwei@gig.ac.cn Orcid https://orcid.org/0000-0002-3750-4208
† Orcid https://orcid.org/0000-0003-3041-7299
‡ Orcid https://orcid.org/0000-0002-9002-4457
§ Orcid https://orcid.org/0000-0001-5929-0709

0003-004X/25/0005–791$05.00/DOI: https://doi.org/10.2138/am-2024-9374

plausible mechanism to explain the notable variations observed in martian hematite. In particular, ground-based telescopic spectral observations suggest that Al-hematite may be present in multiple “bright regions” scattered across the surface of Mars (Morris et al. 1992). Also, some hematite in Gale crater (e.g., the sample Stoer) has relatively smaller *a* and *c* cell parameters, suggesting that there may be significant Al substitution in hematite (Rampe et al. 2020). The widespread occurrence of hematite in ancient martian rocks, along with the potential presence of Al-hematite, may serve as an indicator of soil moisture and pedogenic processes, which are in turn related to climate variability and environments on Mars (Jiang et al. 2022).

The substitution of Al in hematite is influenced by various physicochemical conditions, including temperature and pH (Schwertmann et al. 1979, 2000a; Cornell and Schwertmann 2003). According to experimental studies, a weakly alkaline environment—typically with a pH around 7–8—favors the formation of Al-rich hematite (Schwertmann et al. 1979, 2000a). In addition, several studies have highlighted the significant role of hydrologic conditions in shaping the kinetics, processes, and products of weathering of minerals and rocks by regulating the redox, moisture, and flow rate of surficial and underground waters (Rimstidt and Newcomb 1993; Olsen and Rimstidt 2007; Dixon et al. 2015; Fang et al. 2019; Huang et al. 2021; Zhao et al. 2023). Nevertheless, the precise correlation between hydrologic factors and the formation and preservation of Al-hematite remains uncertain.

Given that the surface of Mars primarily consists of basaltic materials (Rogers and Christensen 2007; Baker 2017; Hadnott et al. 2017), the widespread occurrence of hematite in basaltic laterites on Hainan Island, South China (Long et al. 2011) can serve as an analog for the development of hematite on the mafic to ultramafic crust of Mars. In this study, we used X-ray diffraction (XRD), visible and near-infrared (VNIR) spectroscopy, scanning electron microscopy (SEM), high-resolution transmission electron microscopy (HRTEM), thermogravimetric analysis (TGA), and chemical analyses to investigate the distribution and characteristics of (Al)-hematite in the Hainan basaltic laterite. In addition, we prepared a series of hematite samples with varying Al content in the laboratory and systematically examined their XRD patterns to explore the link between changes in XRD features and the levels of Al substitution in hematite. The heterogeneous distribution of manganese (Mn), cerium (Ce), and gibbsite serves as effective proxies for assessing the hydrologic regime within the laterite. This enables us to investigate the underlying effects of the hydrologic regime on the formation and preservation of Al-hematite. The application of VNIR spectroscopy facilitates a comprehensive analysis of the spectral signatures linked to Al substitution in hematite. This analysis proves valuable in interpreting remote sensing data gathered from Mars. This understanding not only improves our knowledge of terrestrial weathering processes but also enables us to infer the paleoenvironmental conditions that may have existed on Mars.

STUDY AREA AND SAMPLING

Hainan basaltic laterite

The study area is situated on Hainan Island, South China (Fig. 1a). The Cenozoic basalts have a wide distribution across Hainan Island, covering an area of ~4160 km^2. These basalts were deposited over a time period ranging from 100 000 years to 10 million years and can be found in strata that are up to 1 km thick.

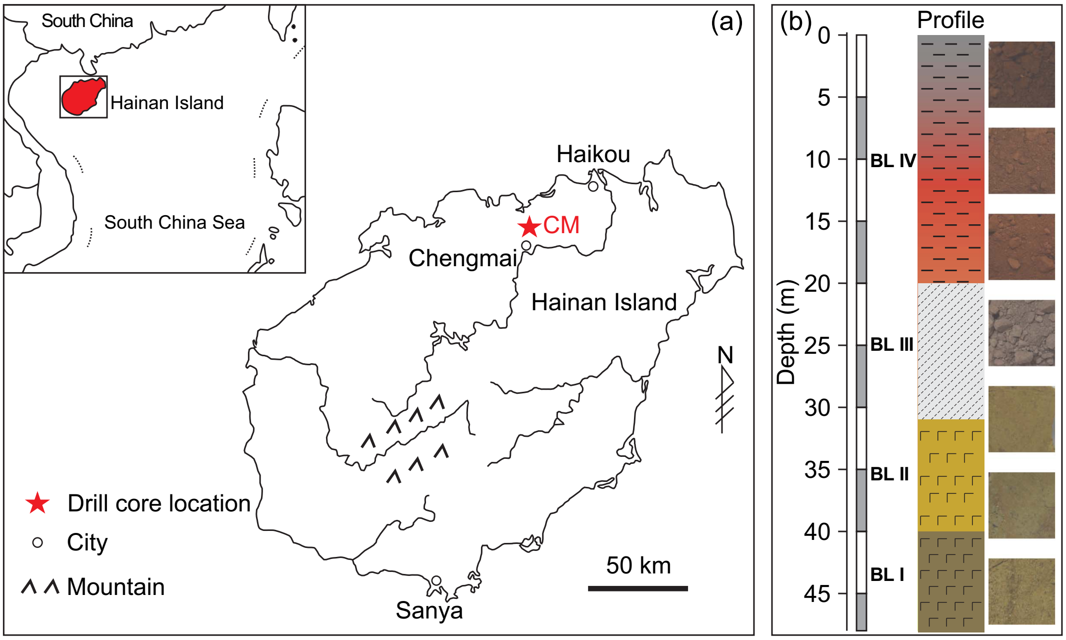

FIGURE 1. (**a**) Simplified geological map of Hainan Island, South China, and the location of the Chengmai basaltic laterite (red star). (**b**) Section of Chengmai basaltic laterite (after Liu et al. 2021a). The laterite is classified as basaltic weathering layer I (BL I), from 48.0 to 39.0 m, basaltic weathering layer II (BL II), from 39.0 to 31.5 m, basaltic weathering layer III (BL III), from 31.5 to 20.0 m, and basaltic weathering layer IV (BL IV), from 20.0 to 1.0 m. The colors and fills in (**b**) correspond to different lithological zones. (Color online.)

The studied area has a warm climate (mean annual temperature ~23.7 °C) and considerable precipitation (mean annual rainfall ~1760 mm), largely influenced by the East Asian Summer Monsoon. Hainan Island exhibits a multitude of basaltic formations, which have given rise to several basaltic laterites that vary in thickness from tens to hundreds of meters.

Sampling

The basaltic laterite being studied is located in the north of Chengmai (CM: 19°46′ 34″N, 110°00′ 23″E), southwest of Haikou City (Fig. 1a). The CM basaltic laterite is ~48 m thick and is composed of a semi-weathered zone (Zone C: 48.0–39.0 m), a completely weathered zone (Zone B: 39.0–5.0 m), and a humic zone (Zone A: 5.0–1.0 m) (Liu et al. 2021a). The CM basaltic laterite is believed to consist of four separate protoliths. Accordingly, the laterite can be subdivided into basaltic weathering layer I (48.0 to 39.0 m), layer II (39.0 to 31.5 m), layer III (31.5 to 20.0 m), and the uppermost layer IV (20.0 to 1.0 m) (Fig. 1b) (Liu et al. 2021a). The investigated samples were collected at 1.0 m intervals from the layer IV, which is inferred to have developed from homogeneous quartz tholeiites, based on the composition of the weathering products. The collected samples were dried at room temperature. The gathered specimens were desiccated at ambient temperature. Subsequently, every sample was powdered to a particle size smaller than 75 μm.

Synthetic Al-hematite samples

Al-hematite samples were prepared using the methods of Li et al. (2016). A specific quantity of $Fe(NO_3)_3{\cdot}9H_2O$ and $Al(NO_3)_3{\cdot}9H_2O$ [with Al/(Al+Fe) values of 0, 0.03, 0.05, 0.07, 0.09, 0.11, and 0.13] was dissolved in 500 mL of deionized water at 90 °C, and 300 mL KOH solution (1 mol L^{-1}) and 50 mL $NaHCO_3$ solution (1 mol L^{-1}) were sequentially added into the solution. The mixture was then placed in an oven and held at a temperature of 90 °C for 96 h. Then, a specific amount of ammonium oxalate was added to the mixture to eliminate the amorphous components and impurities. The obtained samples were washed three times with deionized water, followed by freeze-drying, grinding, and storage in a desiccator. The obtained samples were denoted as AlH-X, in which X represents Al/(Al+Fe) ratio of the initial substance. Each AlH-X sample (10 mg) was weighed and added to 20 mL of HCl solution (6 mol L^{-1}) and heated at 70 °C for 12 h in an oven. The obtained solutions were analyzed using ICP-OES to determine the Al/(Al+Fe) ratio of the resulting AlH-X products.

ANALYTICAL METHODS

X-ray diffraction (XRD)

The mineral composition and abundance analyses were performed using a Rigaku MiniFlex-400 X-ray diffractometer at the Key Laboratory of Mineralogy and Metallogeny of the Guangzhou Institute of Geochemistry, Chinese Academy of Sciences. The diffractometer is equipped with a Hybrid pixel array detector, a Cu source, and a Ni filter. The diffractometer operated with a current of 15 mA and a voltage of 40 kV. All samples were prepared by compacting ground powder materials onto slides for bulk powder analysis. The XRD patterns were obtained by scanning the sample from 3° to 70° (2θ) at a scanning rate of 10° per min and a step size of 0.01°. The JADE 6.5 software was used to calculate the full-width at half maximum (W) and intensity (I) of the given peak specified for each mineral phase.

Major and trace element analysis

Major elements [Al_2O_3, TFe_2O_3 (total iron expressed as Fe_2O_3), SiO_2, K_2O, Na_2O, CaO, MgO, and MnO] were determined by wavelength-dispersive X-ray fluorescence spectrometry (XRF) of fused glass beads. Approximately 0.66 g of each combusted sample was mixed with $Li_2B_4O_7$- $LiBO_2$ (66:34) flux containing 4% $LiNO_3$ and fused into glass disks at 1050 °C. The abundances of major elements in the fused glass disks were measured using a PANalytical PW2424 X-ray fluorescence spectrometer, which has an analytical accuracy and precision of <1% for major element oxides.

The trace elements of bulk powder samples from Hainan basaltic laterite were analyzed using a Thermo Icap Qc inductively coupled plasma-mass spectrometer (ICP-MS). About 0.04 g of sample was digested with a mixture of HNO_3-HF-$HClO_4$ in a closed polytetrafluoroethylene (Teflon) beaker and heated. The digested samples were dried and then fully redissolved with HCl for trace element measurements using an Agilent 7900 ICP-MS. A rhodium standard solution was used as an internal standard to calibrate the machine drift during the measurements. External calibrations based on several United States Geological Survey and Chinese rock and sediment standards (GSR-2, GSR-3, GSD-09, GSD-11, SARM-4, W-2, and AGV-2) were used as reference materials for quality control.

pH value determination

Each powder sample (5.0 g) from the Hainan basaltic laterite was fully mixed with 12.5 g of Milli-Q double deionized water (with a resistivity of 18.25 MΩ cm^{-1}) in a capped beaker for a duration of 1–3 h. The pH values of the powder samples were determined by measuring the filtered liquid three times using a Mettler-Toledo FiveEasy Plus pH meter at room temperature.

Scanning electron microscopy (SEM)

Three thin sections were made from hand specimen samples taken from the laterite at depths of 14.0, 8.0, and 1.0 m for petrographic examination and mineral identification. Each section was then placed in a vacuum carbon evaporator and coated with a thin layer of conductive carbon. The synthetic Al-hematite samples were first dispersed in deionized water and dispersed ultrasonically for ~30 min, and then the sample was collected by transferring a drop of the dispersed solution onto a conductive adhesive, which was subsequently dried in air. The samples were examined using an Analytical Scanning Electron Microscope (TESCAN MIRA 3) and a field emission Scanning Electron Microscope (Hitachi SU8010). The backscattered electron (BSE) and secondary electron images (SEI), and semiquantitative chemical analyses were obtained by energy-dispersive X-ray spectrometry (EDS). The SEM was operated at an accelerating voltage of 20 kV, maintaining a working distance of 15–16 mm.

High-resolution transmission electron microscopy (HRTEM)

The Al contents of hematite particles from the Hainan basaltic laterite were determined using high-resolution transmission electron microscopy (HRTEM). Each powdered sample was first dispersed in an ethanol solution and dispersed ultrasonically for ~10 min. Afterward, a drop of the dispersed solution was transferred onto a porous carbon film supported by a copper grid, which was subsequently air-dried. HRTEM observation was performed on an FEI Talos F200S microscope (Brno, Czech Republic) equipped with an X–ray energy-dispersive detector at the Key Laboratory of Mineralogy and Metallogeny of the Guangzhou Institute of Geochemistry, Chinese Academy of Sciences. The instrument was operated at an accelerating voltage of 200 kV.

Visible and near-infrared (VNIR) spectroscopy

CM laterite samples were analyzed with VNIR to assess the effect of Al-substitution on the spectral features of hematite and provide standards for possible comparative studies to martian data. The powdered samples were measured using an Analytical Spectral Devices FieldSpec-3 spectrometer equipped with a circle detector, and the spot size was ~20 mm. Laboratory measurements were conducted in a dark room under a standard atmosphere, and reflectance was measured relative to a white plate. Acquisitions of 100 scans were used to yield an average spectrum for each measured spectrum to improve the signal-to-noise ratio. The incident angle was 45°, and the emission angle was 0°. ViewSpecPro (version 6.0) software was used to preprocess the raw spectra, including splice correction and averaging. The position of absorption at around

900 nm (P900) was defined by the position of the reflectance minimum between 800 and 1000 nm without continuum removal (Liu et al. 2021a).

RESULTS

Mineralogical and morphology characteristics of synthetic Al-hematite

XRD patterns of the synthesized Al-hematite samples displayed a series of reflections at ∼0.37 nm (24.31°2θ), ∼0.27 nm (33.27°2θ), ∼0.25 nm (35.83°2θ), ∼0.22 nm (41.11°2θ), ∼0.18 nm (49.77°2θ), ∼0.17 nm (54.32°2θ), ∼0.15 nm (62.73°2θ), and ∼0.14 nm (64.34°2θ) (Fig. 2), consistent with the XRD pattern of α-Fe$_2$O$_3$ (PDF#33-0664). With increasing Al content (Online Materials[1] Table S1), the relative intensities (I) and full-width at half maximum (W) of hematite reflections displayed systematic changes (Fig. 2b). The ratio of the intensity of (110) reflection to the intensity of (104) reflection [(I(110)/I(104)] gradually increases from 0.81 for AlH-0 to 1.88 for AlH-13 (Fig. 3a); whereas the ratio of the full-width at half maximum of (110) reflection to the full-width at half maximum of (104) reflection [W(110)/W(104)] decreases from 0.74 for AlH-0 to 0.41 for AlH-13 (Fig. 3b).

The SEM and HRTEM images of synthetic Al-hematite samples are presented in Online Materials[1] Figures S1 and S2. For the samples with low Al content (AlH-0 and AlH-3), the morphology presents as rhombohedral in shape. With increasing Al content, the morphology transforms from rhombohedral to a disk-shaped plate (AlH-7 and AlH-13), with a larger diameter (Online Materials[1] Fig. S3) and a smaller thickness (Online Materials[1] Fig. S4). In particular, the average diameters of AlH-0, AlH-3, AlH-5, AlH-7, AlH-9, AlH-11, and AlH-13 are 71 ± 13, 94 ± 16, 107 ± 13, 126 ± 20, 143 ± 29, 188 ± 24, and 213 ± 36 nm, respectively (Online Materials[1] Fig. S3). The average thickness of AlH-5, AlH-7, AlH-9, AlH-11, and AlH-13 are 17 ± 3, 16 ± 3, 14 ± 3, 9 ± 2, and 5 ± 1 nm, respectively (Online Materials[1] Fig. S4). The particle thickness of AlH-0 and AlH-3 are generally larger than 20 nm (Online Materials[1] Fig. S1).

Mineral and chemical composition of the basalt layer IV

The basalt layer IV is ∼20.0 m thick and can be divided into two distinct sections. The first section, denoted as Section I, spans a depth range of 20.0 to 10.0 m. Above Section I lies Section II, which extends from 10.0 to 1.0 m. Samples from Section I have a deep reddish color and are characterized by a porous structure. The XRD patterns of samples from Section I reveal distinct and discernible reflections (Fig. 4). Notably, sharp reflections at ∼0.34 nm indicate the presence of quartz. Furthermore, a characteristic (001) reflection at ∼0.72 nm signifies the presence of kaolinite. Additionally, reflections at ∼0.27 and ∼0.25 nm correspond to the (104) and (110) crystallographic

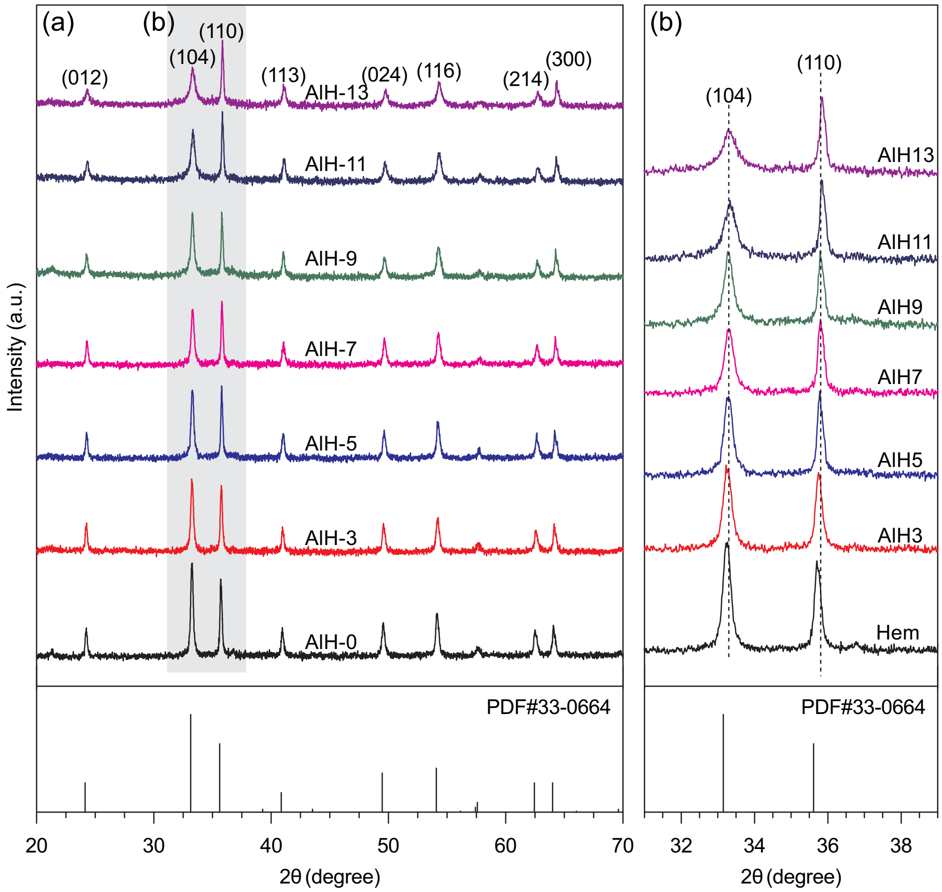

FIGURE 2. (**a**) XRD patterns for synthetic Al-hematite; (**b**) The XRD patterns between 31° and 39° (2θ) display the (104) and (110) diffraction peaks of synthetic Al-hematite, derived from the shadowed area in (**a**). Reference patterns: hematite (α-Fe$_2$O$_3$), PDF#33-0664. (Color online.)

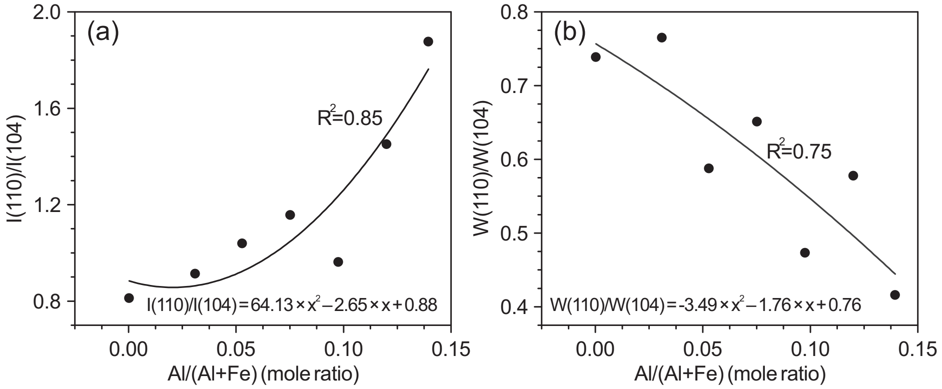

FIGURE 3. Plots of (**a**) I(110)/I(104) and (**b**) W(110)/W(104) vs. Al/(Al+Fe) of synthetic Al-hematite.

planes of hematite, respectively. The semiquantitative analyses suggest that quartz varies in abundance between ~20 to ~50 wt%, while the abundance of kaolinite gradually increases from ~35 wt% at 20.0 m to ~59 wt% at 10.0 m (Fig. 5). The abundance of hematite fluctuates between 10 and 20 wt% (Fig. 5). Compositionally, these samples generally contain low K_2O (0.01–0.03 wt%), Na_2O (0.01–0.04 wt%), CaO (0.01~0.03 wt%), and MgO (0.12–0.55 wt%). In addition. these samples are high in Al_2O_3 (23.45–26.55 wt%), TFe_2O_3 (16.00–20.79 wt%), and SiO_2 (38.19–47.43 wt%) (Online Materials[1] Fig. S5).

The XRD patterns of Section II samples also display distinct reflections at ~0.34, ~0.72, ~0.27, and ~0.25 nm (Fig. 4), which correspond to quartz, kaolinite, and hematite. Samples from Section II exhibit a reflection in their XRD patterns at d-values of ~0.49 nm (Fig. 4), corresponding to the (002) reflections of gibbsite. Notably, as we ascend upwards within Section II, the intensities of this reflection gradually increase (Fig. 4), and the abundance of gibbsite increases from ~3 to ~20 wt% (Fig. 5). Semiquantitative analyses reveal the abundance of quartz fluctuates between 10 and 35 wt% throughout Section II. The

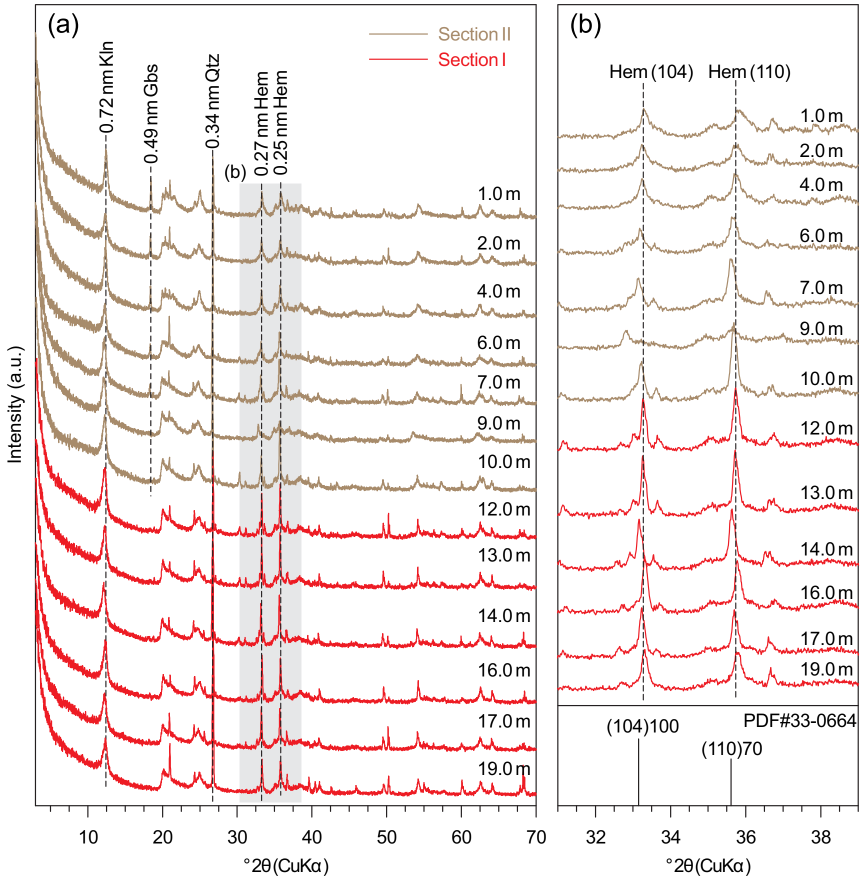

FIGURE 4. (**a**) XRD patterns of representative samples from the basalt layer IV. (**b**) The X-ray diffraction patterns between 31° and 39° (2θ) display the (104) and (110) diffraction peaks of hematite, derived from the shadowed area in (**a**). The relative intensities of (104) and (110) diffraction peaks of hematite gradually change from bottom to top of the laterite compared to the α-Fe_2O_3 (PDF#33-0664). Abbreviations: Kln = kaolinite; Gbs = gibbsite; Qtz = quartz; Hem = hematite. (Color online.)

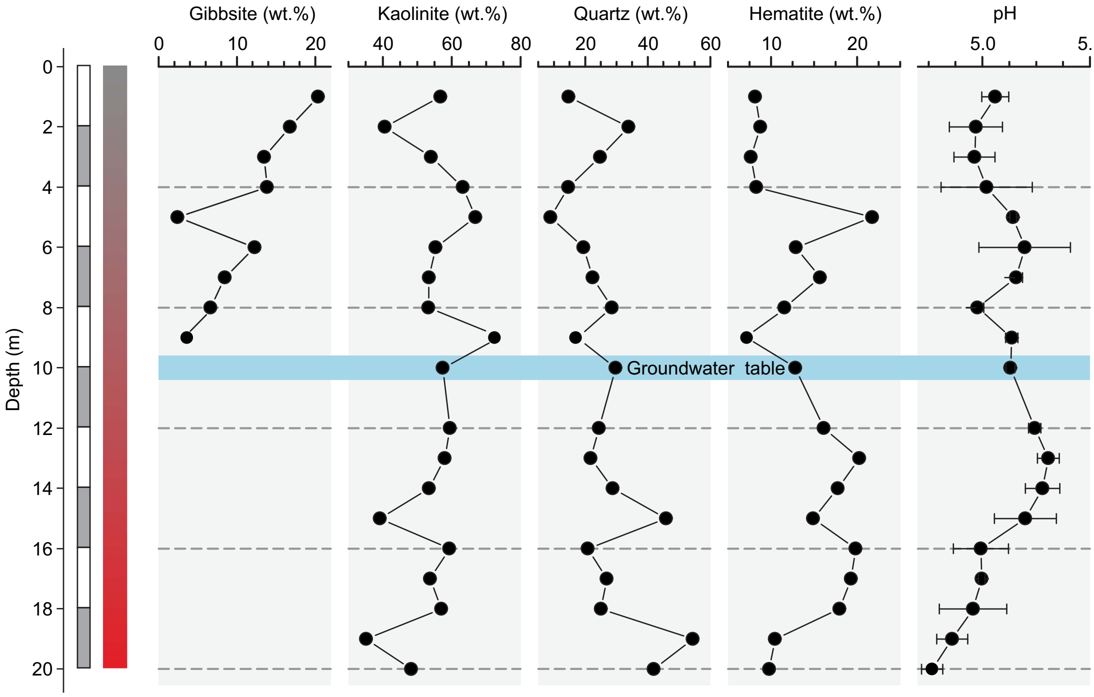

Figure 5. Vertical variations in the content of gibbsite, kaolinite, quartz, hematite, and pH value in the bulk samples as a function of depth in the basalt layer IV. (Color online.)

presence of quartz posed little effect on the formation and preservation of Al-hematite, as quartz is a weathering-resistant mineral present throughout the whole laterite. From bottom to top, the abundance of kaolinite shows a subtle decreasing trend, gradually declining from ~59 to ~40 wt% within this section (Fig. 5). The abundance of hematite within Section II fluctuates, ranging from 5 to 20 wt%. For the samples from Section II, K_2O ranges from 0.01 to 0.18 wt%, Na_2O ranges from 0.02 to 0.04 wt%, CaO is present in trace amounts at 0.01 wt%, and MgO ranges from 0.14 to 0.55 wt% (Online Materials[1] Fig. S5). The samples have high Al_2O_3 (26.26 to 29.05 wt%), TFe_2O_3 (18.34 to 20.93 wt%), and SiO_2 (36.17 to 39.00 wt%) (Online Materials[1] Fig. S5). Meanwhile, the pH values within the laterite fluctuate, ranging from 4.7 to 5.3 (Fig. 5). These pH values indicate a slightly acidic environment within the laterite.

The quartz observed in Sections I and II are likely primary phenocrysts of the protolith. The angular shape of these quartz particles suggests that they were not likely involved in reactions with ambient solutions during the weathering of basalt layer IV, probably due to the insolubility of quartz under near-neutral to acidic conditions (McLennan 2003). In addition, bulk SiO_2 content gradually decreases upwards in the laterite (Online Materials[1] Fig. S5), suggesting the silica released by other weathered silicate minerals was readily leached away. Thereby, the soluble silica was not likely precipitated as secondary quartz and, therefore, did not affect the formation of Al-hematite.

The evaluation of weathering intensities within the laterite relies upon two indices: the "chemical index of alteration" (CIA) and the "index of lateralization" (IOL). These indices use the major element concentrations of whole-rock samples from various depths within the laterite. The CIA is calculated as $CIA = Al_2O_3/[Al_2O_3 + K_2O + Na_2O + CaO] \times 100$ (molar proportions were used according to the definition) (Nesbitt and Young 1982) and the IOL is determined by $IOL = (Al_2O_3 + TFe_2O_3)/(Al_2O_3 + TFe_2O_3 + SiO_2) \times 100$ (mass proportions were used according to the definition) (Babechuk et al. 2014). Overall, samples from the laterite have CIA values above 99, indicating a highly weathered zone (Fig. 6). All samples have CIA values exceeding 99%, making it challenging to differentiate the degree of alteration. Therefore, we used the IOL to measure the weathering intensity in this work. IOL gradually increases upward in the regolith, ranging from 30 to 40 (Fig. 6), indicating a gradually enhanced chemical weathering.

Distributions of bulk-rock Mn and Ce in the profile

Both Mn and Ce are sensitive to the redox state of water environments (Ma et al. 2007; Lanza et al. 2016). Therefore, the distributions of MnO and Ce contents can indicate changes in the redox conditions within the laterite (Koppi et al. 1996; Lanza et al. 2016; Li et al. 2023), which has been linked to the location of the groundwater table (Huang et al. 2021; Peiffer et al. 2021). The Ce anomaly, expressed as $\delta Ce = Ce_N/(La_N \times Pr_N)^{1/2}$ (Ichimura et al. 2020), serves as a valuable tool in distinguishing the redox behavior of Ce relative to its neighboring rare earth elements. This anomaly acts as a fingerprint, allowing us to differentiate between oxic (oxidizing) and anoxic (reducing) conditions (Liu et al. 2019; Ichimura et al. 2020; Wilmeth et al. 2022; Li et al. 2023). Values <1 and >1 represent "negative" and "positive" δCe, respectively. In general, consistently positive δCe points to generally oxic conditions, whereas negative δCe denotes more anoxic conditions (Zhao et al. 2023).

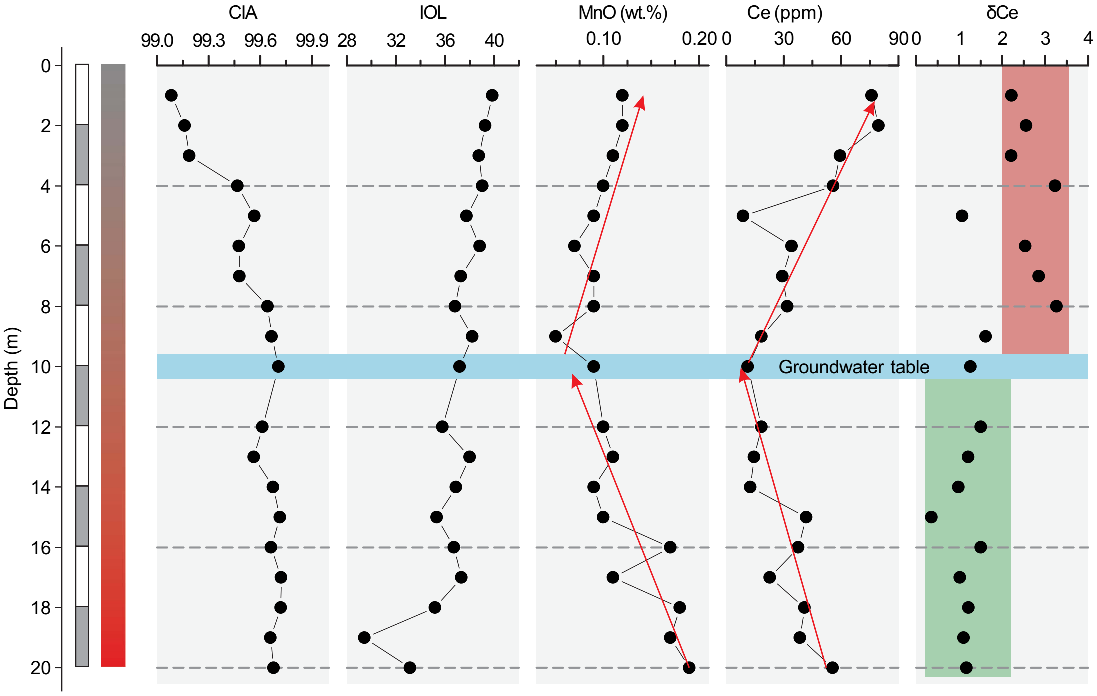

Figure 6. Vertical variations of CIA, IOL, MnO content (wt%), Ce content (ppm), and δCe value in the bulk samples as a function of depth in the basalt layer IV. $\delta Ce = Ce_N/(La_N \times Pr_N)^{1/2}$, where N is C1-chondrite normalized (McDonough and Sun 1995). The blue, green, and red areas represent the groundwater table, anoxic, and oxidizing environments, respectively. (Color online.)

The MnO content decreases gradually from 0.19 wt% at a depth of 20.0 m to 0.09 wt% at a depth of 10.0 m. The MnO content then gradually increases upward, reaching 0.12 wt% at the surface of the laterite (Fig. 6). Notably, the Ce concentration gradually decreases upward from ~55.7 parts per million (ppm) at a depth of 20.0 m to ~11.2 ppm at 10.0 m. This observed decrease in Ce concentration indicates a progressive depletion of Ce within Section II of the profile. In contrast to Section II, the Section I samples exhibit gradually increasing Ce concentrations within this interval, from ~11.2 to ~79.7 ppm (Fig. 6). In all, the distributions of MnO and Ce exhibit similar variation trends (Fig. 6; Online Materials[1] Fig. S6). It is worth noting that the δCe within the laterite exhibits distinct patterns above and below 10.0 m (Fig. 6). Above this boundary, the δCe values are generally >1.5, ranging from 1.5 to 3.7. Conversely, below the boundary, the δCe are generally <1.5, ranging from 0.4 to 1.5 (Fig. 6).

Morphological and crystallographic characteristics of (Al-) hematite

The samples from depths of 1.0, 8.0, and 14.0 m were analyzed using SEM (Fig. 7) and HRTEM (Fig. 8). The SEM images revealed that the hematite grains in the samples from 14.0 m depth were widely distributed and appeared mottled and bright (Figs. 7a–7c). Additionally, the hematite grains were found near the edges of the kaolinite grains (Fig. 7a), and the morphology of the hematite grains is rhombohedral (e.g., Fig. 7b, yellow arrow). Furthermore, the phenocrysts (e.g., pyroxene) within the basalt have completely weathered into hematite, as evidenced by its skeletal texture (Fig. 7c). According to the TEM-EDS results, local areas of the samples from 14.0 m were enriched in Fe, while Al and Si are relatively low (Fig. 8a). The fast Fourier transform (FFT) pattern obtained from the local areas (Figs. 8b–8c) confirms that the iron oxides present are hematite. The Si:Al ratio of kaolinite is close to 1:1, and the calculated mole ratio of Al/(Al+Fe) for hematite can be as low as ~0.02 (Fig. 8d).

The SEM images reveal that the hematite in samples from 8.0 m depth (Figs. 7d–7f) exhibits disk-shaped plate morphologies (e.g., Fig. 7e, yellow arrow), which are notably different from the samples taken at a depth of 14.0 m (e.g., Fig. 7b, yellow arrow). Based on the TEM-EDS results, local areas appear to exhibit enrichment of Fe and Al, while Si is lower (Fig. 8e). Furthermore, hematite particles were identified in the Fe-Al-rich and Si-poor areas through HRTEM and FFT pattern analysis (Figs. 8f–8g). The hematite has a relatively high Al content, with a calculated Al/(Al+Fe) ratio of ~0.17 (Fig. 8h).

The SEM images of the samples taken at a depth of 1.0 m (Figs. 7g–7i) revealed the morphologies of hematite are rhombohedral (e.g., Fig. 7h, yellow arrow), similar to the hematite found at 14.0 m (e.g., Fig. 7b, yellow arrow). According to the TEM-EDS results, Fe is enriched in local areas, where Al and Si are relatively low (Fig. 8i). Hematite particles were identified in the Fe-rich, Al-Si-poor areas using HRTEM and FFT pattern analysis (Figs. 8j–8k). The calculated Al/(Al+Fe) mole ratio for the 1.0 m sample is ~0.01 (Fig. 8l). The Al content of hematite in the 1.0 m sample is lower than that of the 8.0 m sample but similar to that of the 14.0 m sample (Fig. 8).

The XRD patterns of all samples reveal a distinct array of characteristic reflections of the (104) at d-values of ~0.27 nm and reflections of the (110) at ~0.25 nm, respectively (Fig. 4b). The ratio of W(110) to W(104), denoted as W(110)/W(104),

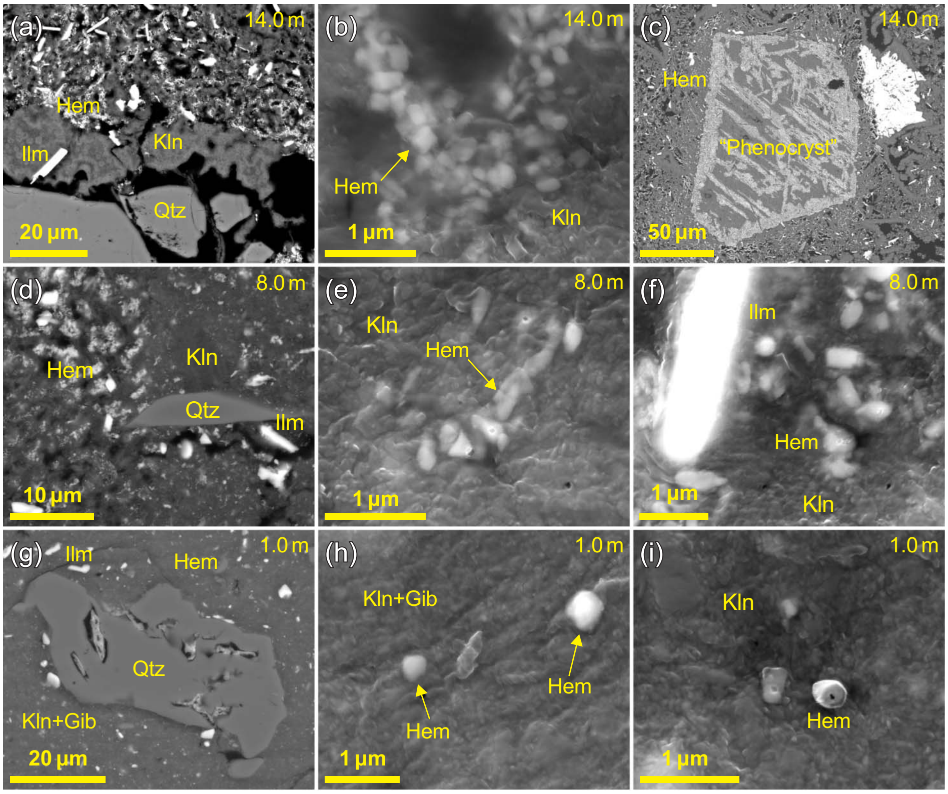

FIGURE 7. Scanning electron microscopy images of primary and supergene minerals of samples from 14.0 m (**a–c**), 8.0 m (**d–f**), and 1.0 m (**g–i**) in the laterite. The dark, angular grains are quartz (Qtz), the dark interstitial phases are kaolinite (Kln) and gibbsite (Gib), and the lath-shaped, bright grains are ilmenite (Ilm) and mottled hematite (Hem). Mottled, bright hematite grains are widely distributed in the samples and near the kaolinite grains' edge or in the fracture-filling of quartz particles. (Color online.)

gradually increases from a depth of 10.0 m upwards to 1.0 m, but does not display any significant changes within the 20.0 to 10.0 m interval (Fig. 9). The ratio of I(110) to I(104), denoted as I(110)/I(104), decreases gradually within the 10.0 to 1.0 m depth interval of the profile. However, within the 20.0 to 10.0 m interval, the W(110) to W(104) and the I(110)/I(104) ratios remain relatively constant (Fig. 9). Furthermore, a negative correlation is observed between the W(110)/W(104) and I(110)/I(104) ratios (Fig. 10a, $R^2 = 0.53$).

VNIR spectral features of (Al-)hematite

The VNIR spectra exhibit an absorption band at ~900 nm (Fig. 11), corresponding to the electron transitions of Fe^{3+} (6A1 → 4T1) in Fe-oxides, specifically hematite and goethite (Townsend 1987). Within the laterite, the position of absorption at ~900 nm (P900) was observed to be ~860 nm in the 20.0–10.0 m range (Figs. 11b and 9) and ~950 nm for the 10.0–1.0 m range and demonstrated a gradual decrease (Figs. 11b and 9). Furthermore, there was a positive correlation between P900 and the I(110)/I(104) ratio (Fig. 10b, $R^2 = 0.54$).

DISCUSSION

Effects of Al substitution on the morphology and crystallographic features of hematite

The substitution of Al has been observed to promote the anisotropic growth of hematite, resulting in noticeable changes in its morphology (Barron et al. 1984; Jiang et al. 2012, 2022; Li et al. 2016). In particular, highly substituted hematite particles have ~3 times larger platelets than non-substituted hematite, while their thickness can decrease by ~25% (Barron et al. 1984; Jiang et al. 2022). The synthetic Al-hematite morphologies change from rhombohedral to disk-shaped plates (Online Materials[1] Figs. S1–S2), with larger diameters but smaller platelet thickness as Al substitution increases (Online Materials[1] Figs. S3–S4).

The anisotropic growth of hematite is characterized by the (104) and (110) reflections in their XRD patterns (Schwertmann et al. 1979; Barron et al. 1984; Jiang et al. 2012; Li et al. 2016). W(110)/W(104) serves as an indicator of the thickness/diameter ratio of hematite crystals (Schwertmann et al. 1979; Barron et al. 1984; Jiang et al. 2012). With increasing Al content in the synthetic Al-hematite, the I(110)/I(104) ratio increases (Fig. 3a), while W(110)/W(104) decreases (Fig. 3b). Mathematically, a polynomial fit of the relative intensity of the (110) and (104) peaks [I(110)/I(104)] displays a quadratic form as $I(110)/I(104) = 64.13 \times x^2 - 2.65 \times x + 0.88$ ($R^2 = 0.85$). The W(110)/W(104) as a function of the Al concentration was fitted via a polynomial relationship $W(110)/W(104) = -3.49 \times x^2 - 1.76 \times x + 0.76$ ($R^2 = 0.75$). Accordingly, the Al content of natural hematite can be quantified by analyzing the ratios of I(110)/I(104) and W(110)/W(104).

Al content of hematite in Hainan basaltic laterite

In the Hainan basaltic laterite, the W(110)/W(104) ratio gradually increases from 10.0 to 1.0 m (Fig. 9), indicating that a gradual increase in the thickness/diameter of hematite and a corresponding decrease in the Al content of hematite. Additionally, the I(110)/I(104) ratio gradually decreases upward (Fig. 9),

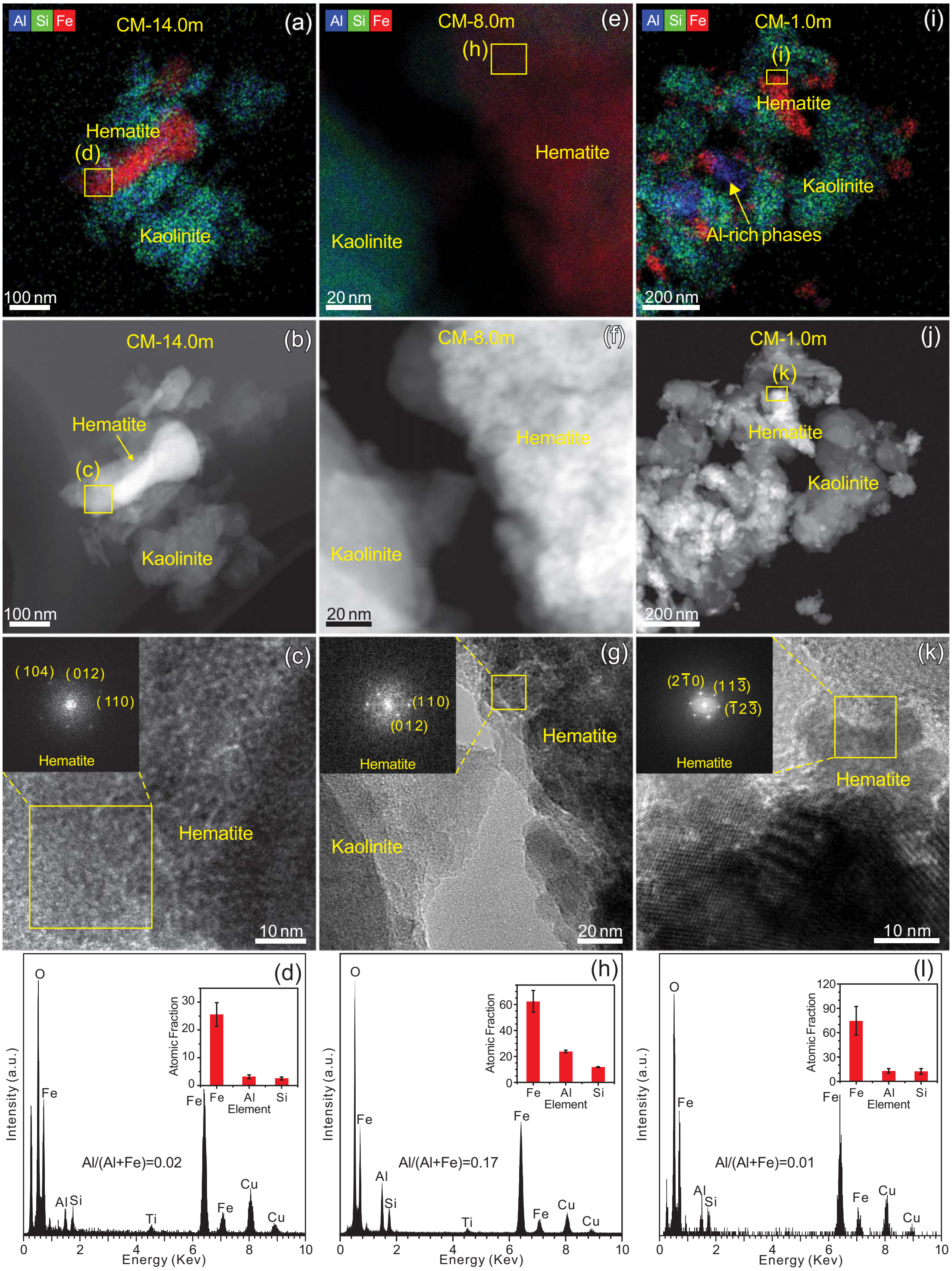

FIGURE 8. HRTEM analyses of hematite from 14.0 m (**a**–**d**), 8.0 m (**e**–**h**), and 1.0 m (**i**–**l**) in the laterite. (**a**) EDS mapping and (**b**) HAADF-STEM images of samples at 14.0 m. (**c**) The corresponding HRTEM image of the selected area (yellow rectangular) in (**b**) shows a single crystal hematite, as confirmed by the inset FFT patterns. (**d**) The corresponding EDS spectrum of the selected area in (**a**) reveals that the Al/(Al+Fe) mole ratio for the hematite is ~0.02. (**e**) EDS mapping and (**f**) HAADF-STEM images of samples in 8.0 m. (**g**) The corresponding HRTEM image of (**f**) shows a single-crystal hematite, as confirmed by the inset FFT patterns. (**h**) The corresponding EDS spectrum of the selected area in (**e**) reveals that the Al/(Al+Fe) mole ratio for the hematite is ~0.17. (**i**) EDS mapping and (**j**) HAADF-STEM images of samples in 1.0 m. (**k**) The corresponding HRTEM image of the selected area (yellow rectangular) in (**j**) shows a single crystal hematite, as confirmed by the inset FFT patterns. (**l**) The corresponding EDS spectrum of the selected area in (**i**) reveals that the Al/(Al+Fe) mole ratio for the hematite is ~0.02. (Color online.)

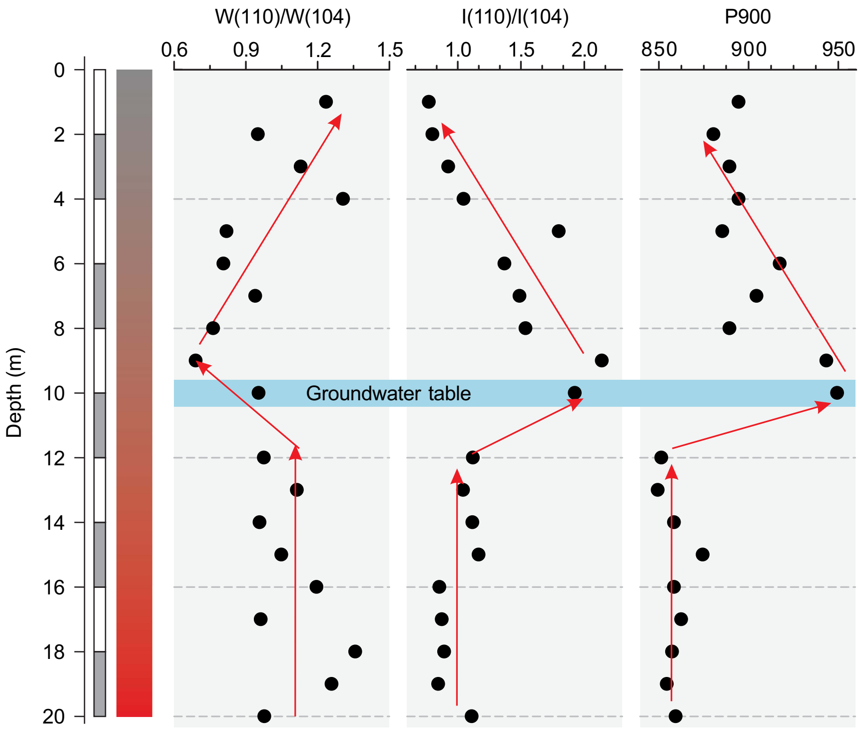

FIGURE 9. Vertical variations in the ratios of the full-width at half maximum of (110) peak to the full-width at half maximum of (104) peak [W(110)/W(104)] and the ratios of the intensity of (110) peak to the intensity of (104) peak [I(110)/I(104)] of hematite. Vertical variations in the visible short-wave infrared reflectance spectral parameters (P900) derived from the crystal-field absorption of Fe^{3+} along the basalt layer IV. (Color online.)

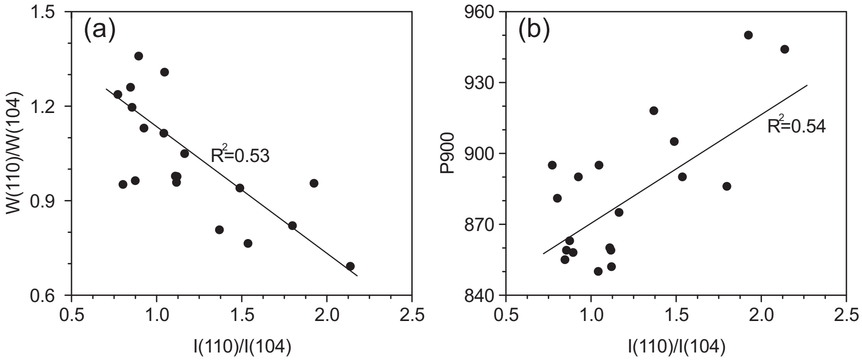

FIGURE 10. Correlations between (**a**) W(110)/W(104) and I(110)/I(104); (**b**) P900 and I(110)/I(104).

indicating a gradual transformation of hematite's crystal morphology to rhombohedral (Li et al. 2016). This transformation coincides with a decrease in the Al content of hematite, similar to what is observed in our synthetic hematite (Fig. 3a). The SEM and HRTEM analyses (Figs. 7–8) indicate that the hematite morphologies gradually change from disk-shaped plates (e.g., Fig. 7e) to rhombohedral shapes (e.g., Fig. 7h) as the Al content decreases. This phenomenon aligns with the findings from synthetic Al-hematite (Online Materials[1] Figs. S1 and S2), indicating that Al substitution is likely the main factor contributing to the formation of plate-like hematite in soils (Liu and Osseo-Asare 2000; Li et al. 2016).

However, the I(110)/I(104) and W(110)/W(104) ratios of the Section I samples are consistent with each other and resemble those of the 1.0 m samples (Fig. 9). This suggests that the hematite morphologies of the Section I samples remain unchanged and similar to the samples at a depth of 1.0 m (Barron et al. 1984; Li et al. 2016). Indeed, the SEM images reveal that the hematite morphologies in the Section I samples exhibit rhombohedral shapes (Fig. 7b), similar to those observed in the 1.0 m samples (Fig. 7h). This rhombohedral morphology is consistent with Al-poor hematite (Schwertmann et al. 1979; Barron et al. 1984; Li et al. 2016), as well as our synthetic Al-poor hematite (Online Materials[1] Fig. S1, AlH-0 and AlH-3). These findings suggest that the hematite within Section I has a lower Al content, as is supported by the observation that the hematite at both 14.0 and 1.0 m depth has Al/(Al+Fe) as low as ~0.02 (Fig. 8d) and ~0.01 (Fig. 8l).

Based on our synthetic Al-hematite (Fig. 3), the variations in the W(110)/W(104) and I(110)/I(104) ratios of hematite within basalt layer IV in Hainan basaltic laterite (Fig. 9) indicate a gradual decrease in Al content from 10.0 to 1.0 m. However, within the range of 20.0–10.0 m, the Al content remains stable and low. The negative correlation between I(110)/I(104) and

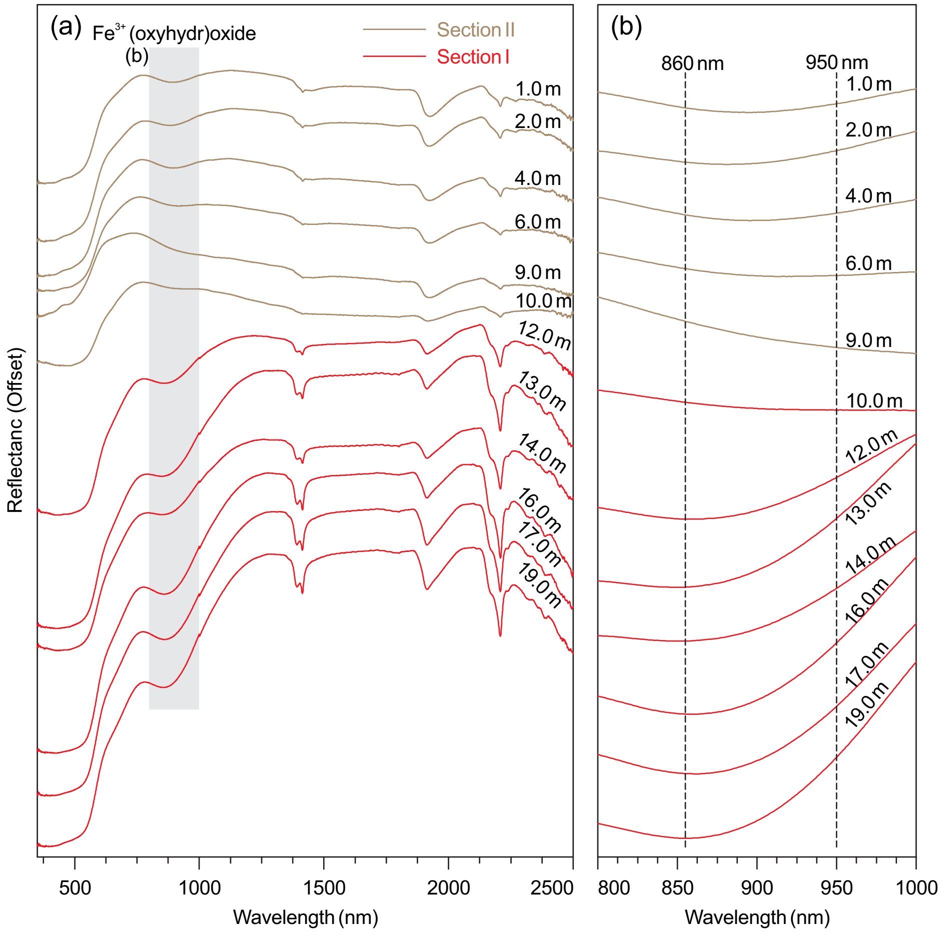

FIGURE 11. (a) Original visible short-wave infrared reflectance spectra (350–2500 nm) of samples from the basalt layer IV; **(b)** Reflectance spectra of Fe (hydr)oxides at the band of 800–1000 nm, derived from the left-shadowed area in **(a)**. (Color online.)

W(110)/W(104) (Fig. 10a, $R^2 = 0.53$) provides further support for this conclusion.

Hydrologic conditions throughout the basaltic laterite

Understanding the hydrologic condition is crucial for comprehending and identifying the hydrologic factors that contribute to the formation and preservation of Al-hematite. Since the recent development of geological structures such as faults can disturb the preexisting hydrological system (Gao et al. 2018; Long et al. 2019), borehole observations may not provide accurate information about the hydrologic conditions at the time of the formation of a laterite (Jaunat et al. 2016). The present study suggests that geochemical and mineralogical indicators, such as the distribution of Mn and Ce, as well as the presence of gibbsite, can provide more reliable information for identifying the location of the groundwater table, assessing water flow rate, and exploring their connection with the formation and preservation of Al-hematite.

Proxies for groundwater table in the basaltic laterite. Ce^{3+} and Mn^{2+} ions are soluble in reduced environments but become insoluble when they are oxidized to Ce^{4+} and $Mn^{3+/4+}$ in oxygen-rich environments (Ma et al. 2007; Abellan et al. 2017; Liu et al. 2019; Li et al. 2023). Hence, the distribution patterns of Mn and Ce in the laterite offer reliable indicators of the redox states (Lanza et al. 2014, 2016; Noda et al. 2019; Ichimura et al. 2020; Wilmeth et al. 2022), which relate to the location of the groundwater table (McQueen and Scott 2009; Huang et al. 2021).

In the laterite, the content of MnO and Ce progressively decreases from 20.0 to 10.0 m (Fig. 6), suggesting that Mn and Ce within the 20.0–10.0 m profile were leached downward as Mn^{2+} and Ce^{3+} in solution under relatively reducing conditions. Correspondingly, below the depth of 10.0 m, δCe generally remains below 1.5 (δCe = 0.4–1.5) (Fig. 6), denoting more reducing conditions. In the upper part of the profile, above 10.0 m, Mn and Ce instead undergo oxidation to become insoluble as $Mn^{3+/4+}$ and Ce^{4+} (CeO_2) in the relatively oxygen-rich environment (Fig. 6). In that interval, the δCe value is >1.5 (δCe = 1.5–3.7) (Fig. 6). These observations suggest a significant shift in the oxic and anoxic environments at the depth of 10.0 m (Ichimura et al. 2020; Huang et al. 2021; Wilmeth et al. 2022).

Alternating oxidizing and reducing conditions can occur through hydrological perturbations at hydrological interfaces, particularly in response to groundwater table fluctuations (McQueen and Scott 2009; Peiffer et al. 2021). The regolith is divided into two distinct zones, namely the vadose zone and the saturated zone, by the groundwater table (Huang et al. 2021). The vadose zone typically extends from the soil surface to the groundwater table. Above the groundwater table, gases (including oxygen from the atmosphere) have greater access to the regolith via voids and fractures, and conditions are typically more oxidizing (McQueen and Scott 2009; Holden and Fierer 2005). Therefore, vadose zones generally exhibit relatively high oxygen partial pressure (pO_2 of 2.13×10^4–1.52×10^4 Pa) (Abellan et al. 2017). In contrast, the saturated zone, which lies beneath the groundwater table, is an unconfined aquifer. It primarily contains dissolved oxygen, with a low pO_2 of $\sim 2 \times 10^{-4}$ Pa (Holden and Fierer 2005). As a result, the pronounced shift in the oxic and anoxic environments at the depth of 10.0 m (Fig. 6) can be attributed to the position of the groundwater table. This division separates the profile into relatively oxidizing environments in the vadose zone (10.0–1.0 m) and more reducing environments in the saturated zone (20.0–10.0 m) (Fig. 6).

Distinctive hydrologic conditions in the basaltic laterite. Orbital spectroscopy, along with α-particle X-ray spectroscopy data collected from landing sites, has provided evidence that strongly supports the fundamentally igneous and basaltic composition of the upper crust on Mars. Further, plagioclase and pyroxene are the dominant minerals of martian basalt (Bandfield et al. 2004), a composition that resembles the observed mineral composition on Hainan Island. It is, therefore, likely that the alteration of pyroxene and feldspar leads to the dissolution of Fe, Al, and Si into the solution, ultimately allowing the formation of secondary minerals such as Fe-oxides and Al-rich kaolinite. Specifically, it is hypothesized that martian hematite is formed through in situ weathering of precursor silicate materials under oxidizing conditions (Fraeman et al. 2013). Such a scenario aligns with the formation process of hematite observed in Hainan Island (Fig. 7c). Considering the insolubility of quartz under near-neutral to acidic conditions (McLennan 2003), the presence or absence of quartz has minimal direct influence on the transformation of precursor silicate materials into hematite. Therefore, the formation process of hematite observed in Hainan Island can serve as an analog for understanding the development of hematite on the mafic to ultramafic crust of Mars. The apparent scarcity of abundant quartz in martian weathering settings may be attributed to various causes, including different initial lithologies (with more quartz in terrestrial equivalents), and the inability of orbital spectroscopy to detect quartz directly (Wray et al. 2013).

The CIA values of all samples exceed 99 (Fig. 6), suggesting a high level of weathering (Mohanty et al. 2016). During the weathering of basalt, the alteration of mafic phenocrysts, such as pyroxene, results in the release of Fe and Si into the solution. Additionally, the alteration of felsic glassy substance and feldspar releases Al and Si. These reactions are involved in the creation of (Al-)hematite, kaolinite, and gibbsite (Fig. 5). Nevertheless, gibbsite is solely present in the vadose zone and completely absent in the saturated zone (Fig. 5). Previous studies have indicated that the precipitation of gibbsite from dissolved K-feldspar and kaolinite only happens when the concentration of total dissolved silica decreases to levels below 10^{-6} and $10^{-4.6}$ $mol \cdot L^{-1}$, respectively (Gardner 1970, 1972). According to the equivalent porous media model proposed by Jaunat et al. (2016), the permeability of the saturated zone is roughly 100 times lower than that of the vadose zone. Hence, the presence of gibbsite in the vadose zone (Fig. 5) suggests that the dissolved silica can be readily leached away by infiltrating water. In contrast, the formation of gibbsite was impeded in the saturated zone (Fig. 5), suggesting that the removal of dissolved silica was not as efficient. Consequently, water in the vadose zone exhibits a relatively high flow rate, while water in the saturated zone has a comparatively low flow rate (McQueen and Scott 2009).

Heterogeneous distribution of (Al-)hematite controlled by hydrologic conditions

The distribution of (Al-)hematite may be influenced by factors such as mineral compositions, pH levels, and the intensity of weathering. Nevertheless, there is a poor correlation between I(110)/I(104) and pH (Fig. 12a, $R^2 = 0.12$), Al/(Al+Fe) of whole-rock samples (Fig. 12b, $R^2 = 0.16$), CIA (Fig. 12c, $R^2 = 0.11$), and the quantity of kaolinite (Fig. 12d, $R^2 = 0.27$). This observation suggests that these parameters may not account for the variations in the Al content of hematite (Fig. 9). In addition, the temperature remains approximately constant above 20 m in laterite (Mao et al. 2023), indicating that temperature has a limited effect on the Al content of hematite in laterite. It is intriguing to note that there is a correlation between the inferred groundwater table and the fluctuation in hematite Al content (Fig. 9). This suggests that the hydrologic circumstances play a key role in the creation and preservation of Al-hematite.

Favorable environment for formation of (Al-)hematite. The water in the saturated zone maintains a consistent state with a comparatively sluggish rate of movement (McQueen and Scott 2009; Gleeson et al. 2016; Arora et al. 2019). The relatively reduced flow rate hinders the process of Si^{4+} leaching from the laterite. Consequently, Al^{3+} and Si^{4+} tend to co-precipitate, resulting in the formation of Al, Si-rich phases like kaolinite (Fig. 4). This causes the residual solids to have a lower concentration of Al^{3+}, resulting in the absence of Al-rich, Si-poor phases, such as gibbsite [$Al(OH)_3$] (Fig. 4). Similarly, the more sluggish movement of water in the saturated zone also obstructs the transportation of Fe^{2+} from the dissolved phenocrysts of pyroxene. This leads to the in situ oxidation of Fe^{2+} and the formation of hematite as a pseudomorph (Fig. 7c). During this process, the low concentration of Al^{3+} in the residual solids results in hematite with a low Al^{3+} content (Figs. 8a–8d). Consequently, the aerobic weathering of basalt in a stable water environment with a relatively slower flow rate facilitates the formation of Al-poor hematite (Figs. 13d–13e).

In contrast, the vadose zone would be transiently filled with relatively oxidized percolated meteoric water but tends to become dry due to the relatively high flow rate of water in the vadose zone (McQueen and Scott 2009; Jaunat et al. 2016). The high water flux in the vadose zone results in substantial leaching of Si^{4+} due to its higher mobility relative to Al^{3+}, making the residual solids enriched in Al^{3+} but depleted in Si^{4+} as weathering progresses. This is further confirmed by the occurrence of Al-rich phases, such as gibbsite $Al(OH)_3$ (Fig. 4). The relatively higher water flow rate in the vadose zone also promoted the leaching of Fe^{2+} from the phenocrysts. The Fe^{2+} that enters the ambient solution can subsequently undergo oxidation through the reaction with oxygen and precipitate as hematite. The crystallization of hematite from Fe^{3+} was increased by the alternating wet and dry conditions in the vadose zone (Buggle et al. 2014; Zhao et al. 2017). The fast crystallization process is thermodynamically advantageous (Wang and Xu 2001; Yang et al. 2022) for the incorporation of Al^{3+} into the structure of hematite. Consequently, the Al^{3+} tended to co-precipitate with Fe^{3+} and form

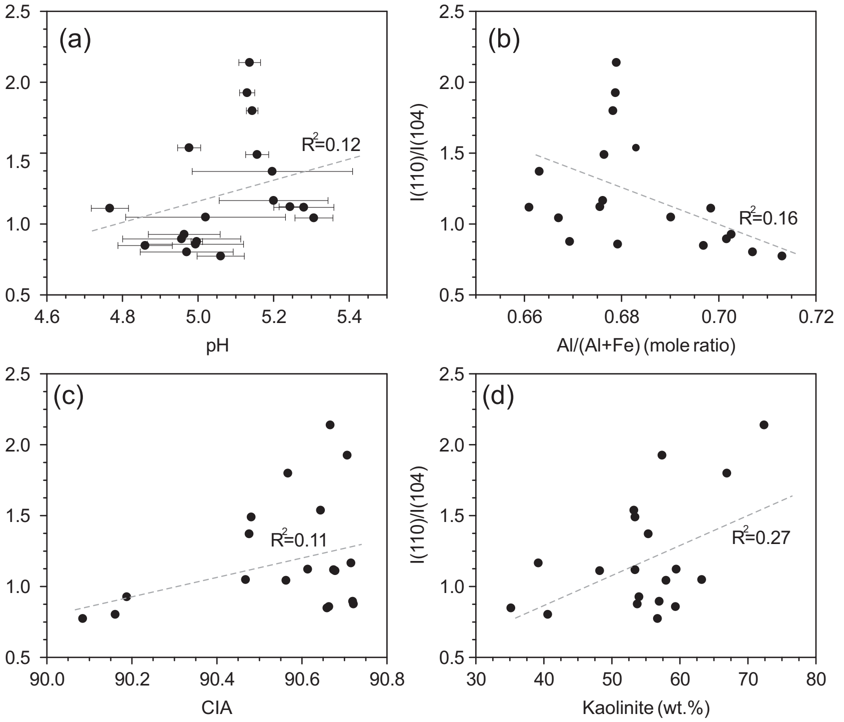

FIGURE 12. Plots of I(110)/I(104) vs. (**a**) pH, (**b**) Al/(Al+Fe), (**c**) CIA, and (**d**) the content of kaolinite of basalt layer IV, whole-rock samples.

uniformly dispersed Al-hematite within the vadose zone (Figs. 8e–8h). In summary, a water environment characterized by a high flow rate and alternating wet and dry regime is favorable for the formation of Al-rich hematite (Figs. 13a–13c).

Favorable environment for preservation of Al-hematite. In the vadose zone of the laterite, the Al content in the hematite dropped progressively toward the upper layers (Fig. 9), leading to the development of Al-poor hematite at the surface (Fig. 8). Usually, the meteoric water that seeps into the topsoil can be held in place by capillary forces, thereby creating a zone that is abundant in "soil water." The existence of "soil water" might account for the transformation of Al-rich hematite into Al-poor hematite (Figs. 13f–13g).

Al is not compatible with the crystal structure of hematite ($\alpha\text{-Fe}_2^{3+}O_3$), which results in the relatively low crystallinity of Al-hematite (Morris et al. 1992; Jiang et al. 2022). In general, incompatible elements tend to gradually migrate out of the crystal lattice of host minerals during the process of re-crystallization. This migration serves to reduce the Gibbs free energy inside the mineral system (Yang et al. 2022). Importantly, water flow has a crucial role in directing the recrystallization process of poorly crystallized minerals (Tosca and Knoll 2009). Thus, the existence of "soil water" plays a crucial role in driving the recrystallization of Al-rich hematite, leading to the formation of Al-poor hematite at the topsoil. This observation suggests that the preservation of Al-rich hematite is largely dependent on the limited duration of water presence (Figs. 13f–13g).

VNIR spectroscopic features of (Al-)hematite as indicators of hydrologic environment on Mars

VNIR spectroscopy is a commonly used technique to detect and analyze the mineralogy of Mars (Cuadros et al. 2016; Jeute et al. 2021; Pineau et al. 2022). The features observed between 850–950 nm are primarily attributed to the electron transitions of Fe^{3+} in Fe oxides, such as hematite and goethite (Bell et al. 1990; Cudahy and Ramanaidou 1997; Cuadros et al. 2020). The variation of P900 (Fig. 11b) depends on the Al content of hematite and/or the relative concentrations of hematite and goethite in the samples (Morris et al. 1992; Cudahy and Ramanaidou 1997; Liu et al. 2021a).

Goethite generally forms in persistently moist environments via direct precipitation from solution (Zhao et al. 2017). Our results demonstrate that such a scenario is unfavorable for the formation of Al-rich hematite (Fig. 9 and 13). Therefore, the abundant coexistence of goethite and Al-hematite should be quite unlikely on Mars. In addition, the VNIR spectrum of goethite includes Fe^{3+} bands near 640–730 nm, while hematite shows minimal absorption at ~700 nm (Online Materials[1] Fig. S9). Accordingly, these spectral features near 640–730 nm can be used to ascertain the presence of goethite on the surface of Mars. In this scenario, the VNIR spectra collected from locations with a high goethite abundance should exhibit evident absorption near 640–730 nm. Additionally, only Al-poor hematite could be present in these locations.

In contrast, the extent of P900s fluctuation is mostly determined by the Al content of hematite, rather than the quantity of goethite, in cases when the absorption band near 640–730 nm is absent. For example, the XRD (Fig. 4) and TG (Online Materials[1] Fig. S7–S8) analyses indicate the absence of goethite in the investigated laterite. Therefore, analyses from this study suggest that the shift in P900 could mostly be ascribed to variations in the Al content of hematite. The positive correlations between P900 and I(110)/I(104) (Fig. 10b, $R^2 = 0.54$) show that P900 shifts toward longer wavelengths as the Al content of hematite increases,

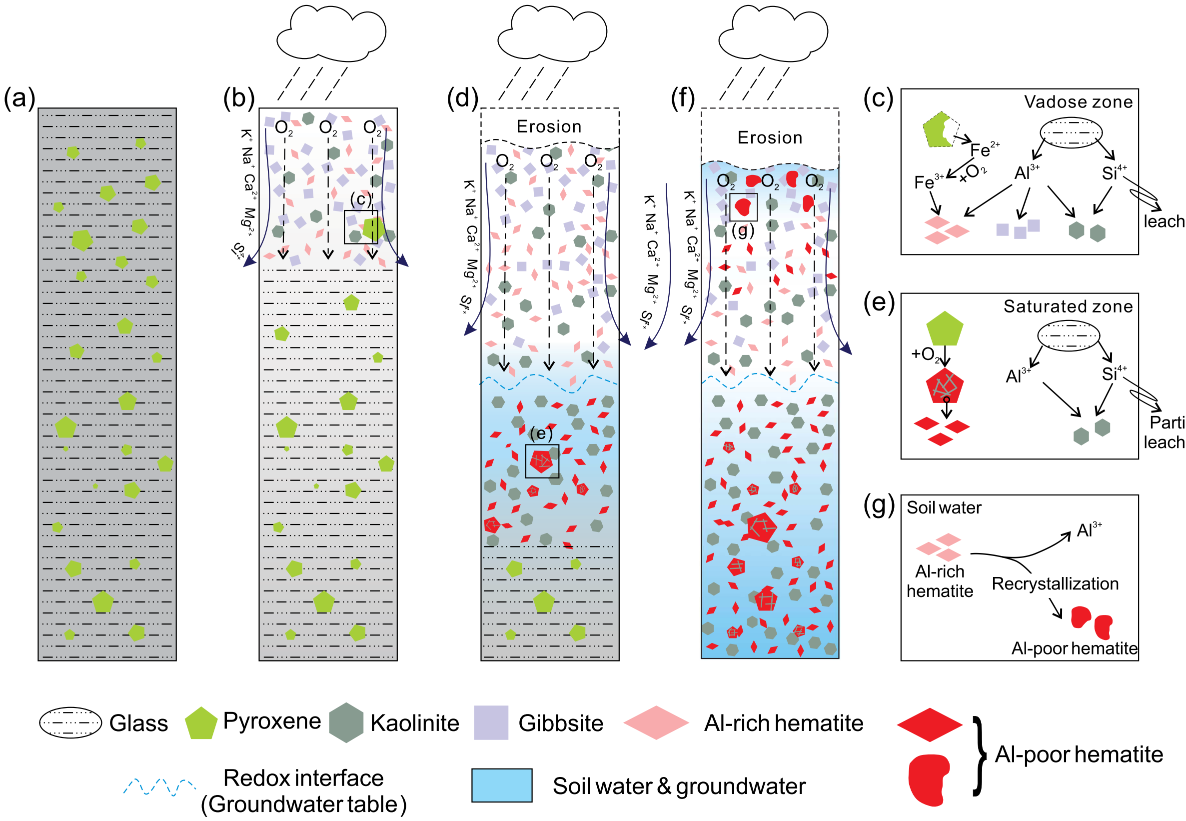

Figure 13. Illustrations showing a model for the formation and preservation of Al-hematite in the Chengmai basaltic laterite. (**a**–**c**) Higher flow rate and an alternating wet and dry environment led to the formation of Al-rich hematite. (**d**–**e**) The aerobic weathering of basalt under a stable water environment (slightly slower flow rate and liquid water can remain stable) will form Al-poor hematite. (**f**–**g**) The presence of "soil water" serves as a driving force for the recrystallization of Al-rich hematite, ultimately leading to the formation of Al-poor hematite. (Color online.)

the results reported by Morris et al. (1992). Therefore, P900 can effectively determine the Al content of martian hematite.

IMPLICATIONS

Hematite (α-$Fe_2^{3+}O_3$) is the dominant pigment mineral that adorns the surface of Mars, earning the planet its iconic nickname, the "Red Planet" (Bell et al. 1990; Fraeman et al. 2013; Rampe et al. 2020). In the context of Mars discoveries, it has been reported that nanophase, red crystalline, gray crystalline, and Al-rich hematite occurred in certain areas of the martian surface (Morris et al. 1989, 1992; Christensen et al. 2001; Fraeman et al. 2013; Rampe et al. 2020). Previous studies have ascribed the formation of nanophase, red crystalline, and gray crystalline hematite to factors like pH, temperature, and the duration of water present (Bell et al. 1993; Catling and Moore 2003; Barron et al. 2006; Madden et al. 2010; Rampe et al. 2020). Moreover, this study suggests that the substitution of Al can have a significant effect on the mineralogical characteristics of hematite. It can also serve as an indicator of the moisture conditions associated with climate variations on Mars.

Thorough investigations of the characteristics of terrestrial hematite are necessary to establish a basis for understanding hematite found on Mars (Jiang et al. 2022) since sample return from Mars is a long way into the future (Papike et al. 2007). The widespread presence of Al-rich clay minerals (e.g., kaolinite) in the thick weathering profiles (generally 50–60 m) in ancient martian terrains (Gaudin et al. 2011; Bishop et al. 2018; Ye and Michalski 2022) suggests that advanced weathering probably emerged on Mars. Given the presence of hematite in the thick chemical weathering profiles at the Mawrth Vallis (Liu et al. 2021b) and Al-rich hematite possibly occurring in less weathered basalt (CIA value is about 58) at Gale crater (Rampe et al. 2020; Frydenvang et al. 2020), the effects of hydrologic regime on the formation and preservation of Al-hematite in the investigated basaltic laterite (Fig. 13) can serve as systematic analogs to explore the characteristics and genesis of hematite of martian rock with different levels of chemical weathering at different geographical sites.

This study suggests that an alternating wet and dry regime with a high leaching rate of Si is favorable for the formation of Al-rich hematite. Accordingly, the formation of Al-hematite in some martian outcrops could serve as an effective mineralogical proxy for the transient presence of percolating water. In contrast, prolonged chemical interactions between "soil water" and Al-hematite tend to transform Al-rich hematite to Al-poor hematite via re-crystallization. Therefore, Al-hematite could only occur on the martian surface with short-term presence of liquid water, such as episodic floods (Manga 2004) and intense precipitation (Craddock and Lorenz 2017).

The presence of transient liquid water with high flow rates is possibly responsible for the formation of alluvial fans, valley networks, and dendritic channels in the Libya Montes region, together with the absence of phyllosilicates (Bishop et al. 2013, 2018; Wordsworth 2016). Additionally, the presence of transient liquid water also suggests that Mars may have experienced brief periods of warmer and wetter environment in its early history, possibly due to impacts (Segura et al. 2002, 2012; Pan et al. 2023), volcanism (Wordsworth 2016), or seasonal effects (Ojha et al. 2020). Importantly, the occurrence of Al-rich hematite can be assessed using VNIR, a technique available onboard many Mars missions. Using VNIR to detect the potential presence of Al-rich hematite on Mars is important for advancing the investigation of the hydrological conditions on the planet.

ACKNOWLEDGMENTS AND FUNDING

This study was supported by the National Natural Science Foundation of China (Grant No. 41921003, 42272038), the National Science Fund for Distinguished Young Scholars (Grant No. 41825003), the Youth Innovation Promotion Association CAS (Grant No. 2023369), the Science and Technology Planning Project of Guangdong Province, China (Grant No. 2023B1212060048), the Open Project of State Key Laboratory of Lunar and Planetary Science, the Macau University of Science and Technology [Grant No. SKL-LPS(MUST)-2021-2023]. This is contribution No.IS-3638 from GIGCAS. We thank Associate Editor Lindsay McHenry and two anonymous reviewers for their constructive comments that greatly helped improve the manuscript. Xiaoliang Liang and Hui Yin are thanked for their assistance with the synthetic Al-hematite samples.

REFERENCES CITED

Abellan, P., Moser, T.H., Lucas, I.T., Grate, J.W., Evans, J.E., and Browning, N.D. (2017) The formation of cerium(III) hydroxide nanoparticles by a radiation mediated increase in local pH. RSC Advances, 7, 3831–3837, https://doi.org/10.1039/C6RA27066B.

Arora, B., Dwivedi, D., Faybishenko, B., Jana, R.B., and Wainwright, H.M. (2019) Understanding and predicting vadose zone processes. Reviews in Mineralogy and Geochemistry, 85, 303–328, https://doi.org/10.2138/rmg.2019.85.10.

Babechuk, M.G., Widdowson, M., and Kamber, B.S. (2014) Quantifying chemical weathering intensity and trace element release from two contrasting basalt profiles, Deccan Traps, India. Chemical Geology, 363, 56–75, https://doi.org/10.1016/j.chemgeo.2013.10.027.

Baker, L.L. (2017) Formation of the ferruginous smectite SWa-1 by alteration of soil clays. American Mineralogist, 102, 33–41, https://doi.org/10.2138/am-2017-5735.

Bandfield, J.L., Hamilton, V.E., Christensen, P.R., and McSween, H.Y. Jr. (2004) Identification of quartzofeldspathic materials on Mars. JGR Planets, 109, E10009, https://doi.org/10.1029/2004JE002290.

Barron, V., Rendon, J.L., Torrent, J., and Serna, C.J. (1984) Relation of infrared, crystallochemical, and morphological properties of Al-substituted hematites. Clays and Clay Minerals, 32, 475–479, https://doi.org/10.1346/CCMN.1984.0320605.

Barron, V., Torrent, J., and Greenwood, J.P. (2006) Transformation of jarosite to hematite in simulated Martian brines. Earth and Planetary Science Letters, 251, 380–385, https://doi.org/10.1016/j.epsl.2006.09.022.

Bell, J.F. III, McCord, T.B., and Owensby, P.D. (1990) Observational evidence of crystalline iron oxides on Mars. Journal of Geophysical Research: Solid Earth, 95, 14447–14461, https://doi.org/10.1029/JB095iB09p14447.

Bell, J.F. III, Morris, R.V., and Adams, J.B. (1993) Thermally altered palagonitic tephra–A spectral and process analog to the soil and dust of Mars. JGR Planets, 98, 3373–3385, https://doi.org/10.1029/92JE02367.

Bishop, J.L., Tirsch, D., Tornabene, L.L., Jaumann, R., McEwen, A.S., McGuire, P.C., Ody, A., Poulet, F., Clark, R.N., Parente, M., and others. (2013) Mineralogy and morphology of geologic units at Libya Montes, Mars: Ancient aqueously derived outcrops, mafic flows, fluvial features, and impacts. JGR Planets, 118, 487–513, https://doi.org/10.1029/2012JE004151.

Bishop, J.L., Fairén, A.G., Michalski, J.R., Gago-Duport, L., Baker, L.L., Velbel, M.A., Gross, C., and Rampe, E.B. (2018) Surface clay formation during short-term warmer and wetter conditions on a largely cold ancient Mars. Nature Astronomy, 2, 206–213, https://doi.org/10.1038/s41550-017-0377-9.

Buggle, B., Hambach, U., Müller, K., Zöller, L., Marković, S.B., and Glaser, B. (2014) Iron mineralogical proxies and Quaternary climate change in SE-European loess-paleosol sequences. Catena, 117, 4–22, https://doi.org/10.1016/j.catena.2013.06.012.

Catling, D.C. and Moore, J.A. (2003) The nature of coarse-grained crystalline hematite and its implications for the early environment of Mars. Icarus, 165, 277–300, https://doi.org/10.1016/S0019-1035(03)00173-8.

Christensen, P.R., Morris, R.V., Lane, M.D., Bandfield, J.L., and Malin, M.C. (2001) Global mapping of Martian hematite mineral deposits: Remnants of water-driven processes on early Mars. Journal of Geophysical Research: Planets, 106, 23873–23885, https://doi.org/10.1029/2000JE001415.

Cornell, R.M. and Schwertmann, U. (2003) The Iron Oxides: Structure, Properties, Reactions, Occurrences, and Uses, 714 p. Wiley-vch.

Craddock, R.A. and Lorenz, R.D. (2017) The changing nature of rainfall during the early history of Mars. Icarus, 293, 172–179, https://doi.org/10.1016/j.icarus.2017.04.013.

Cuadros, J., Michalski, J.R., Dekov, V., and Bishop, J.L. (2016) Octahedral chemistry of 2:1 clay minerals and hydroxyl band position in the near-infrared: Application to Mars. American Mineralogist, 101, 554–563, https://doi.org/10.2138/am-2016-5366.

Cuadros, J., Sánchez-Marañón, M., Mavris, C., Fiore, S., Bishop, J.L., and Melgosa, M. (2020) Color analysis and detection of Fe minerals in multi-mineral mixtures from acid-alteration environments. Applied Clay Science, 193, 105677, https://doi.org/10.1016/j.clay.2020.105677.

Cudahy, T.J. and Ramanaidou, E.R. (1997) Measurement of the hematite:goethite ratio using field visible and near infrared reflectance spectrometry in channel iron deposits, Western Australia. Australian Journal of Earth Sciences, 44, 411–420, https://doi.org/10.1080/08120099708728322.

Dixon, E.M., Elwood Madden, A.S., Hausrath, E.M., and Elwood Madden, M.E. (2015) Assessing hydrodynamic effects on jarosite dissolution rates, reaction products, and preservation on Mars. JGR Planets, 120, 625–642, https://doi.org/10.1002/2014JE004779.

Fang, Q., Hong, H., Algeo, T.J., Huang, X., Sun, A., Churchman, G.J., Chorover, J., Chen, S., and Liu, Y. (2019) Microtopography-mediated hydrologic environment controls elemental migration and mineral weathering in subalpine surface soils of subtropical monsoonal China. Geoderma, 344, 82–98, https://doi.org/10.1016/j.geoderma.2019.03.008.

Fraeman, A.A., Arvidson, R.E., Catalano, J.G., Grotzinger, J.P., Morris, R.V., Murchie, S.L., Stack, K.M., Humm, D.C., McGovern, J.A., Seelos, F.P., and others. (2013) A hematite-bearing layer in Gale Crater, Mars: Mapping and implications for past aqueous conditions. Geology, 41, 1103–1106, https://doi.org/10.1130/G34613.1.

Frydenvang, J., Mangold, N., Wiens, R.C., Fraeman, A.A., Edgar, L.A., Fedo, C.M., L'Haridon, J., Bedford, C.C., Gupta, S., Grotzinger, J.P., and others (2020) The chemostratigraphy of the Murray formation and role of diagenesis at Vera Rubin ridge in Gale crater, Mars, as observed by the ChemCam instrument. JGR Planets, 125, e2019JE006320.

Gao, Q., Shang, Y., Hasan, M., Jin, W., and Yang, P. (2018) Evaluation of a weathered rock aquifer using ERT method in South Guangdong, China. Water, 10, 293, https://doi.org/10.3390/w10030293.

Gardner, L.R. (1970) A chemical model for the origin of gibbsite from kaolinite. American Mineralogist, 55, 1380–1389.

——— (1972) Conditions for direct formation of gibbsite from K-feldspar—Further discussion. American Mineralogist, 57, 294–300.

Gaudin, A., Dehouck, E., and Mangold, N. (2011) Evidence for weathering on early Mars from a comparison with terrestrial weathering profiles. Icarus, 216, 257–268, https://doi.org/10.1016/j.icarus.2011.09.004.

Gleeson, T., Befus, K.M., Jasechko, S., Luijendijk, E., and Cardenas, M.B. (2016) The global volume and distribution of modern groundwater. Nature Geoscience, 9, 161–167, https://doi.org/10.1038/ngeo2590.

Hadnott, B.A., Ehlmann, B.L., and Jolliff, B.L. (2017) Mineralogy and chemistry of San Carlos high-alkali basalts: Analyses of alteration with application for Mars exploration. American Mineralogist, 102, 284–301, https://doi.org/10.2138/am-2017-5608.

Holden, P.A. and Fierer, N. (2005) Microbial processes in the vadose zone. Vadose Zone Journal, 4, 1–21, https://doi.org/10.2136/vzj2005.0001.

Hu, P., Jiang, Z., Liu, Q., Heslop, D., Roberts, A.P., Torrent, J., and Barrón, V. (2016) Estimating the concentration of aluminum-substituted hematite and goethite using diffuse reflectance spectrometry and rock magnetism: Feasibility and limitations. Journal of Geophysical Research: Solid Earth, 121, 4180–4194, https://doi.org/10.1002/2015JB012635.

Huang, J., He, H., Tan, W., Liang, X., Ma, L., Wang, Y., Qin, X., and Zhu, J. (2021) Groundwater controls REE mineralisation in the regolith of South China. Chemical Geology, 577, 120295, https://doi.org/10.1016/j.chemgeo.2021.120295.

Ichimura, K., Sanematsu, K., Kon, Y., Takagi, T., and Murakami, T. (2020) REE redistributions during granite weathering: Implications for Ce anomaly as a proxy for paleoredox states. American Mineralogist, 105, 848–859, https://doi.org/10.2138/am-2020-7148.

Jaunat, J., Dupuy, A., Huneau, F., Celle-Jeanton, H., and Le Coustumer, P. (2016) Groundwater flow dynamics of weathered hard-rock aquifers under climate-change conditions: An illustrative example of numerical modeling through the equivalent porous media approach in the north-western Pyrenees (France). Hydrogeology Journal, 24, 1359–1373, https://doi.org/10.1007/s10040-016-1408-9.

Jeute, T., Baker, L.L., Bishop, J.L., Abidin, Z., and Rampe, E.B. (2021) Spectroscopic analysis of allophane and imogolite samples with variable Fe abundance for characterizing the poorly crystalline components on Mars. American Mineralogist, 106, 527–540, https://doi.org/10.2138/am-2020-7329.

Jiang, Z., Liu, Q., Barrón, V., Torrent, J., and Yu, Y. (2012) Magnetic discrimination between Al-substituted hematites synthesized by hydrothermal and thermal dehydration methods and its geological significance. Journal of Geophysical Research: Solid Earth, 117, B02102, https://doi.org/10.1029/2011JB008605.

Jiang, Z., Liu, Q., Roberts, A.P., Dekkers, M.J., Barrón, V., Torrent, J., and Li, S. (2022) The magnetic and color reflectance properties of hematite: From Earth to Mars. Reviews of Geophysics, 60, e2020RG000698.

Koppi, A.J., Edis, R., Field, D.J., Geering, H.R., Klessa, D.A., and Cockayne, D.J.H. (1996) Rare earth element trends and cerium-uranium-manganese associations in weathered rock from Koongarra, northern territory, Australia. Geochimica et Cosmochimica Acta, 60, 1695–1707, https://doi.org/10.1016/0016-7037(96)00047-6.

Lanza, N.L., Fischer, W.W., Wiens, R.C., Grotzinger, J., Ollila, A.M., Cousin, A., Anderson, R.B., Clark, B.C., Gellert, R., Mangold, N., and others. (2014) High manganese concentrations in rocks at Gale crater, Mars. Geophysical Research Letters, 41, 5755–5763, https://doi.org/10.1002/2014GL060329.

Lanza, N.L., Wiens, R.C., Arvidson, R.E., Clark, B.C., Fischer, W.W., Gellert, R., Grotzinger, J.P., Hurowitz, J.A., McLennan, S.M., Morris, R.V., and others. (2016) Oxidation of manganese in an ancient aquifer, Kimberley formation, Gale crater, Mars. Geophysical Research Letters, 43, 7398–7407, https://doi.org/10.1002/2016GL069109.

Li, W., Liang, X., An, P., Feng, X., Tan, W., Qiu, G., Yin, H., and Liu, F. (2016) Mechanisms on the morphology variation of hematite crystals by Al substitution: The modification of Fe and O reticular densities. Scientific Reports, 6, 35960, https://doi.org/10.1038/srep35960.

Li, W., Liu, X., Nakada, R., Takahashi, Y., Hu, Y., Shakouri, M., Zhang, Z., Okumura, T., and Yamada, S. (2023) The cerium isotope fingerprints of redox fluctuation in bauxites. Earth and Planetary Science Letters, 602, 117962, https://doi.org/10.1016/j.epsl.2022.117962.

Liu, Q. and Osseo-Asare, K. (2000) Synthesis of monodisperse Al-substituted hematite particles from highly condensed metal hydroxide gels. Journal of Colloid and Interface Science, 231, 401–403, https://doi.org/10.1006/jcis.2000.7142.

Liu, X., Hardisty, D.S., Lyons, T.W., and Swart, P.K. (2019) Evaluating the fidelity of the cerium paleoredox tracer during variable carbonate diagenesis on the Great Bahamas Bank. Geochimica et Cosmochimica Acta, 248, 25–42, https://doi.org/10.1016/j.gca.2018.12.028.

Liu, J., He, H., Michalski, J.R., Cuadros, J., Yao, Y., Tan, W., Qin, X., Li, S., and Wei, G. (2021a) Reflectance spectroscopy applied to clay mineralogy and alteration intensity of a thick basaltic weathering sequence in Hainan Island, South China. Applied Clay Science, 201, 105923, https://doi.org/10.1016/j.clay.2020.105923.

Liu, J., Michalski, J.R., Tan, W., He, H., Ye, B., and Xiao, L. (2021b) Anoxic chemical weathering under a reducing greenhouse on early Mars. Nature Astronomy, 5, 503–509, https://doi.org/10.1038/s41550-021-01303-5.

Long, X., Ji, J., and Balsam, W. (2011) Rainfall-dependent transformations of iron oxides in a tropical saprolite transect of Hainan Island, South China: Spectral and magnetic measurements. Journal of Geophysical Research. Earth Surface, 116, F03015.

Long, X.T., Zhang, K.N., Yuan, R.Q., Zhang, L., and Liu, Z. (2019) Hydrogeochemical and isotopic constraints on the pattern of a deep circulation groundwater flow System. Energies, 12, 404, https://doi.org/10.3390/en12030404.

Ma, J.L., Wei, G.J., Xu, Y.G., Long, W.G., and Sun, W.D. (2007) Mobilization and re-distribution of major and trace elements during extreme weathering of basalt in Hainan Island, South China. Geochimica et Cosmochimica Acta, 71, 3223–3237, https://doi.org/10.1016/j.gca.2007.03.035.

Madden, A.S., Hamilton, V.E., Elwood Madden, M.E., Larson, P.R., and Miller, M.A. (2010) Low-temperature mechanism for formation of coarse crystalline hematite through nanoparticle aggregation. Earth and Planetary Science Letters, 298, 377–384, https://doi.org/10.1016/j.epsl.2010.08.014.

Manga, M. (2004) Martian floods at Cerberus Fossae can be produced by groundwater discharge. Geophysical Research Letters, 31, L02702, https://doi.org/10.1029/2003GL018958.

Mao, R., Zhao, Z., Tian, L., Fang, T., and Wang, X. (2023) Generation of gridded temperature map of constant-temperature layer based on meteorological data for shallow geothermal applications. Geothermics, 113, 102770, https://doi.org/10.1016/j.geothermics.2023.102770.

McDonough, W.F. and Sun, S.S. (1995) The composition of the earth. Chemical Geology, 120, 223–253, https://doi.org/10.1016/0009-2541(94)00140-4.

McLennan, S.M. (2003) Sedimentary silica on Mars. Geology, 31, 315–318, https://doi.org/10.1130/0091-7613(2003)031<0315:SSOM>2.0.CO;2.

McQueen, K. and Scott, K. (2009) Rock Weathering and Structure of the Regolith. In K. Scott and C. Pain, Eds., Regolith Science, 103–126. CSIRO Publishing.

Mohanty, B., Gupta, A., and Das, B.S. (2016) Estimation of weathering indices using spectral reflectance over visible to mid-infrared region. Geoderma, 266, 111–119, https://doi.org/10.1016/j.geoderma.2015.11.030.

Morris, R.V., Agresti, D.G., Lauer, H.V. Jr., Newcomb, J.A., Shelfer, T.D., and Murali, A.V. (1989) Evidence for pigmentary hematite on Mars based on optical, magnetic, and Mossbauer studies of superparamagnetic (nanocrystalline) hematite. Journal of Geophysical Research: Solid Earth, 94, 2760–2778, https://doi.org/10.1029/JB094iB03p02760.

Morris, R.V., Schulze, D.G., Lauer, H.V. Jr., Agresti, D.G., and Shelfer, T.D. (1992) Reflectivity (visible and near IR), Mössbauer, static magnetic, and X-ray diffraction properties of aluminum-substituted hematites. Journal of Geophysical Research: Solid Earth, 97, 10257–10266, https://doi.org/10.1029/92JE00455.

Nesbitt, H.W. and Young, G.M. (1982) Early Proterozoic climates and plate motions inferred from major element chemistry of lutites. Nature, 299, 715–717, https://doi.org/10.1038/299715a0.

Noda, N., Imamura, S., Sekine, Y., Kurisu, M., Fukushi, K., Terada, N., Uesugi, S., Numako, C., Takahashi, Y., and Hartmann, J. (2019) Highly oxidizing aqueous environments on early Mars inferred from scavenging pattern of trace metals on manganese oxides. JGR Planets, 124, 1282–1295, https://doi.org/10.1029/2018JE005892.

Ojha, L., Buffo, J., Karunatillake, S., and Siegler, M. (2020) Groundwater production from geothermal heating on early Mars and implication for early martian habitability. Science Advance, 6, eabb1669.

Olsen, A.A. and Rimstidt, J.D. (2007) Using a mineral lifetime diagram to evaluate the persistence of olivine on Mars. American Mineralogist, 92, 598–602, https://doi.org/10.2138/am.2007.2462.

Pan, L., Deng, Z., and Bizzarro, M. (2023) Impact induced oxidation and its implications for early Mars climate. Geophysical Research Letters, 50, e2023GL102724.

Papike, J.J., Burger, P.V., Karner, J.M., Shearer, C.K., and Lueth, V.W. (2007) Letter. Terrestrial analogs of martian jarosites: Major, minor element systematics and Na-K zoning in selected samples. American Mineralogist, 92, 444–447, https://doi.org/10.2138/am.2007.2442.

Peiffer, S., Kappler, A., Haderlein, S.B., Schmidt, C., Byrne, J.M., Kleindienst, S., Vogt, C., Richnow, H.H., Obst, M., Angenent, L.T., and others. (2021) A biogeochemical-hydrological framework for the role of redox-active compounds in aquatic systems. Nature Geoscience, 14, 264–272, https://doi.org/10.1038/s41561-021-00742-z.

Pineau, M., Mathian, M., Baron, F., Rondeau, B., Le Deit, L., Allard, T., and Mangold, N. (2022) Estimating kaolinite crystallinity using near-infrared spectroscopy: Implications for its geology on Earth and Mars. American Mineralogist, 107, 1453–1469, https://doi.org/10.2138/am-2022-8025.

Rampe, E.B., Bristow, T.F., Morris, R.V., Morrison, S.M., Achilles, C.N., Ming, D.W., Vaniman, D.T., Blake, D.F., Tu, V.M., Chipera, S.J., and others (2020) Mineralogy of Vera Rubin Ridge from the Mars Science Laboratory CheMin Instrument. Journal of Geophysical Research: Planets, 125, e2019JE006306.

Rimstidt, J.D. and Newcomb, W.D. (1993) Measurement and analysis of rate data: The rate of reaction of ferric iron with pyrite. Geochimica et Cosmochimica Acta, 57, 1919–1934, https://doi.org/10.1016/0016-7037(93)90084-A.

Rogers, A.D. and Christensen, P.R. (2007) Surface mineralogy of martian low albedo regions from MGS-TES data: Implications for upper crustal evolution and surface alteration. Journal of Geophysical Research: Solid Earth, 112, E01003, https://doi.org/10.1029/2006JE002727.

Schwertmann, U. and Murad, E. (1988) The nature of an iron oxide-organic iron association in a peaty environment. Clay Minerals, 23, 291–299, https://doi.org/10.1180/claymin.1988.023.3.06.

Schwertmann, U., Fitzpatrick, R.W., Taylor, R.M., and Lewis, D.G. (1979) The influence of aluminum on iron oxides, part II: Preparation and properties of Al substituted hematites. Clays and Clay Minerals, 27, 105–112, https://doi.org/10.1346/CCMN.1979.0270205.

Schwertmann, U., Friedl, J., Stanjek, H., and Schulze, D.G. (2000a) The effect of Al on Fe oxides. XIX. Formation of Al-substituted hematite from ferrihydrite at 25 °C and pH 4 to 7. Clays and Clay Minerals, 48, 159–172, https://doi.org/10.1346/CCMN.2000.0480202.

——— (2000b) The effect of clay minerals on the formation of goethite and hematite from ferrihydrite after 16 years' ageing at 25 °C and pH 4–7. Clay Minerals, 35, 613–623, https://doi.org/10.1180/000985500547034.

Segura, T.L., Toon, O.B., Colaprete, A., and Zahnle, K. (2002) Environmental effects of large impacts on Mars. Science, 298, 1977–1980, https://doi.org/10.1126/science.1073586.

Segura, T.L., McKay, C.P., and Toon, O.B. (2012) An impact-induced, stable, runaway climate on Mars. Icarus, 220, 144–148, https://doi.org/10.1016/j.icarus.2012.04.013.

Singh, B. and Gilkes, R.J. (1992) Properties and distribution of iron oxides and their association with minor elements in the soils of south-western Australia. Journal of Soil Science, 43, 77–98, https://doi.org/10.1111/j.1365-2389.1992.tb00121.x.

Torrent, J., Guzman, R., and Parra, M.A. (1982) Influence of relative humidity on the crystallization of Fe(III) oxides from ferrihydrite. Clays and Clay Minerals, 30, 337–340, https://doi.org/10.1346/CCMN.1982.0300503.

Tosca, N.J. and Knoll, A.H. (2009) Juvenile chemical sediments and the long term persistence of water at the surface of Mars. Earth and Planetary Science Letters, 286, 379–386, https://doi.org/10.1016/j.epsl.2009.07.004.

Townsend, T.E. (1987) Discrimination of iron alteration minerals in visible and near-infrared reflectance data. Journal of Geophysical Research: Solid Earth, 92, 1441–1454, https://doi.org/10.1029/JB092iB02p01441.

Wang, Y. and Xu, H. (2001) Prediction of trace metal partitioning between minerals and aqueous solutions: A linear free energy correlation approach. Geochimica et Cosmochimica Acta, 65, 1529–1543, https://doi.org/10.1016/S0016-7037(01)00551-8.

Wells, M.A., Fitzpatrick, R.W., Gilkes, R.J., and Dobson, J. (1999) Magnetic properties of metal-substituted haematite. Geophysical Journal International, 138, 571–580, https://doi.org/10.1046/j.1365-246X.1999.00840.x.

Wilmeth, D.T., Lalonde, S.V., Berelson, W.M., Petryshyn, V., Celestian, A.J., Beukes, N.J., Awramik, S.M., Spear, J.R., Mahseredjian, T., and Corsetti, F.A. (2022) Evidence for benthic oxygen production in Neoarchean lacustrine stromatolites. Geology, 50, 907–911, https://doi.org/10.1130/G49894.1.

Wordsworth, R.D. (2016) The climate of early Mars. Annual Review of Earth and Planetary Sciences, 44, 381–408, https://doi.org/10.1146/annurev-earth-060115-012355.

Wray, J.J., Hansen, S.T., Dufek, J., Swayze, G.A., Murchie, S.L., Seelos, F.P., Skok, J.R., Irwin, R.P. III, and Ghiorso, M.S. (2013) Prolonged magmatic activity on Mars inferred from the detection of felsic rocks. Nature Geoscience, 6, 1013–1017, https://doi.org/10.1038/ngeo1994.

Yang, Y., He, H., Tan, W., Tao, Q., Yao, J., Xian, H., Li, S., Xi, J., Zhu, J., and Xu, H. (2022) Incorporation of incompatible trace elements into molybdenite: Layered PbS precipitates within molybdenite. American Mineralogist, 107, 54–64, https://doi.org/10.2138/am-2021-7609.

Ye, B. and Michalski, J.R. (2022) Chemical weathering over hundreds of millions of years of greenhouse conditions on Mars. Communications Earth & Environment, 3, 266, https://doi.org/10.1038/s43247-022-00602-7.

Zhao, L., Hong, H., Fang, Q., Yin, K., Wang, C., Li, Z., Torrent, J., Cheng, F., and Algeo, T.J. (2017) Monsoonal climate evolution in southern China since 1.2 Ma: New constraints from Fe-oxide records in red earth sediments from the Shengli section, Chengdu Basin. Palaeogeography, Palaeoclimatology, Palaeoecology, 473, 1–15, https://doi.org/10.1016/j.palaeo.2017.02.027.

Zhao, L., Hong, H., Fang, Q., Hei, H., and Algeo, T.J. (2023) Hydrologic regulation of clay-mineral transformations in a redoximorphic soil of subtropical monsoonal China. American Mineralogist, 108, 1881–1896, https://doi.org/10.2138/am-2022-8706.

Manuscript received March 1, 2024
Manuscript accepted July 27, 2024
Accepted manuscript online August 12, 2024
Manuscript handled by Lindsay J. McHenry

Endnotes:

[1] Deposit item AM-25-59374. Online Materials are free to all readers. Go online, via the table of contents or article view, and find the tab or link for supplemental materials.